LUND UNIVERSITY

SQSTM1/p62-Directed Metabolic Reprogramming Is Essential for Normal Neurodifferentiation

Calvo-Garrido, Javier; Maffezzini, Camilla; Schober, Florian A; Clemente, Paula; Uhlin, Elias; Kele, Malin; Stranneheim, Henrik; Lesko, Nicole; Bruhn, Helene; Svenningsson, Per; Falk, Anna; Wedell, Anna; Freyer, Christoph; Wredenberg, Anna

LUND UNIVERSITY

PO Box 117
221 00 Lund
+46 46-222 00 00

Download date: 04. Jul. 2025

Stem Cell Reports

Article

SQSTM1/p62-Directed Metabolic Reprogramming Is Essential for Normal Neurodifferentiation

Javier Calvo-Garrido,[1,2,7] Camilla Maffezzini,[1,3,7] Florian A. Schober,[1,2] Paula Clemente,[1,3] Elias Uhlin,[4] Malin Kele,[4] Henrik Stranneheim,[2,5] Nicole Lesko,[3,5] Helene Bruhn,[3,5] Per Svenningsson,[6] Anna Falk,[4] Anna Wedell,[1,2,5,8] Christoph Freyer,[1,3,5,8,*] and Anna Wredenberg[1,3,5,8,*]

[1]Max Planck Institute Biology of Ageing - Karolinska Institutet Laboratory, Karolinska Institutet, 171 65 Stockholm, Sweden
[2]Department of Molecular Medicine and Surgery, Karolinska Institutet, 171 76 Stockholm, Sweden
[3]Department of Medical Biochemistry and Biophysics, Karolinska Institutet, 171 65 Stockholm, Sweden
[4]Department of Neuroscience, Karolinska Institutet, 171 65 Stockholm, Sweden
[5]Centre for Inherited Metabolic Diseases, Karolinska University Hospital, 171 76 Stockholm, Sweden
[6]Department of Clinical Neuroscience, Karolinska Institutet, 171 76 Stockholm, Sweden
[7]Co-first author
[8]Co-senior author
*Correspondence: christoph.freyer@ki.se (C.F.), anna.wredenberg@ki.se (A.W.)
https://doi.org/10.1016/j.stemcr.2019.01.023

SUMMARY

Neurodegenerative disorders are an increasingly common and irreversible burden on society, often affecting the aging population, but their etiology and disease mechanisms are poorly understood. Studying monogenic neurodegenerative diseases with known genetic cause provides an opportunity to understand cellular mechanisms also affected in more complex disorders. We recently reported that loss-of-function mutations in the autophagy adaptor protein SQSTM1/p62 lead to a slowly progressive neurodegenerative disease presenting in childhood. To further elucidate the neuronal involvement, we studied the cellular consequences of loss of p62 in a neuroepithelial stem cell (NESC) model and differentiated neurons derived from reprogrammed p62 patient cells or by CRISPR/Cas9-directed gene editing in NESCs. Transcriptomic and proteomic analyses suggest that p62 is essential for neuronal differentiation by controlling the metabolic shift from aerobic glycolysis to oxidative phosphorylation required for neuronal maturation. This shift is blocked by the failure to sufficiently downregulate lactate dehydrogenase expression due to the loss of p62, possibly through impaired Hif-1α downregulation and increased sensitivity to oxidative stress. The findings imply an important role for p62 in neuronal energy metabolism and particularly in the regulation of the shift between glycolysis and oxidative phosphorylation required for normal neurodifferentiation.

INTRODUCTION

Brain development is a dynamic, complex, and well-organized process that initiates during the third gestational week and continues throughout development until late adolescence. During this period, neuronal differentiation, maturation, and migration are controlled and tightly regulated by carefully coordinated genetic programs (Paridaen and Huttner, 2014). Small changes in cellular environment and metabolic demands affect cellular fate and are often a requirement for correct neuronal maturation (Kim et al., 2014). Even subtle disturbances during any of these processes can result in a number of neurodegenerative disorders, but the complexity of the brain and cellular metabolism has limited our understanding of neuronal homeostasis in health and disease. A small subgroup of neurodegenerative diseases is caused by inborn errors of metabolism (IEM), defined by the toxic accumulation of metabolic intermediates or the lack of vital substrates. IEM are caused by single gene defects, thus affecting specific biochemical pathways, such as carbohydrate, lipid, amino acid, lysosomal, mitochondrial, and peroxisomal metabolism (El-Hattab, 2015). The molecular and metabolic consequences observed in these diseases therefore offer unique opportunities to study the interplay between the genetic and the metabolic demands of the developing brain, providing vital advances in understanding the changes observed in more complex common neurodegenerative disorders.

We recently reported that the loss of the autophagy adaptor Sequestosome 1 (SQSTM1/p62) in nine individuals from four different families leads to a childhood- or adolescence-onset neurodegenerative disorder, characterized by progressive gait abnormalities, ataxia, dysarthria, dystonia, vertical gaze palsy, and cognitive decline (Haack et al., 2016). Magnetic resonance imaging revealed atrophy of the cerebellum and the vermis cerebelli (Haack et al., 2016). Eleven more patients, with similar clinical presentations, have since been reported (Muto et al., 2018). Nevertheless, there was no clear indication of the pathogenetic mechanism leading to the clinical observations. p62 has been associated with several cellular processes, such as selective autophagy (Lamark et al., 2009) and mitophagy (Park et al., 2014), as well as responses to oxidative stress (Jiang et al., 2015), immune response (Lee et al., 2015), and hypoxia (Rantanen et al., 2013). More recently, p62 was also shown to be an important regulator in cancer metabolism, with increased p62 expression reported in
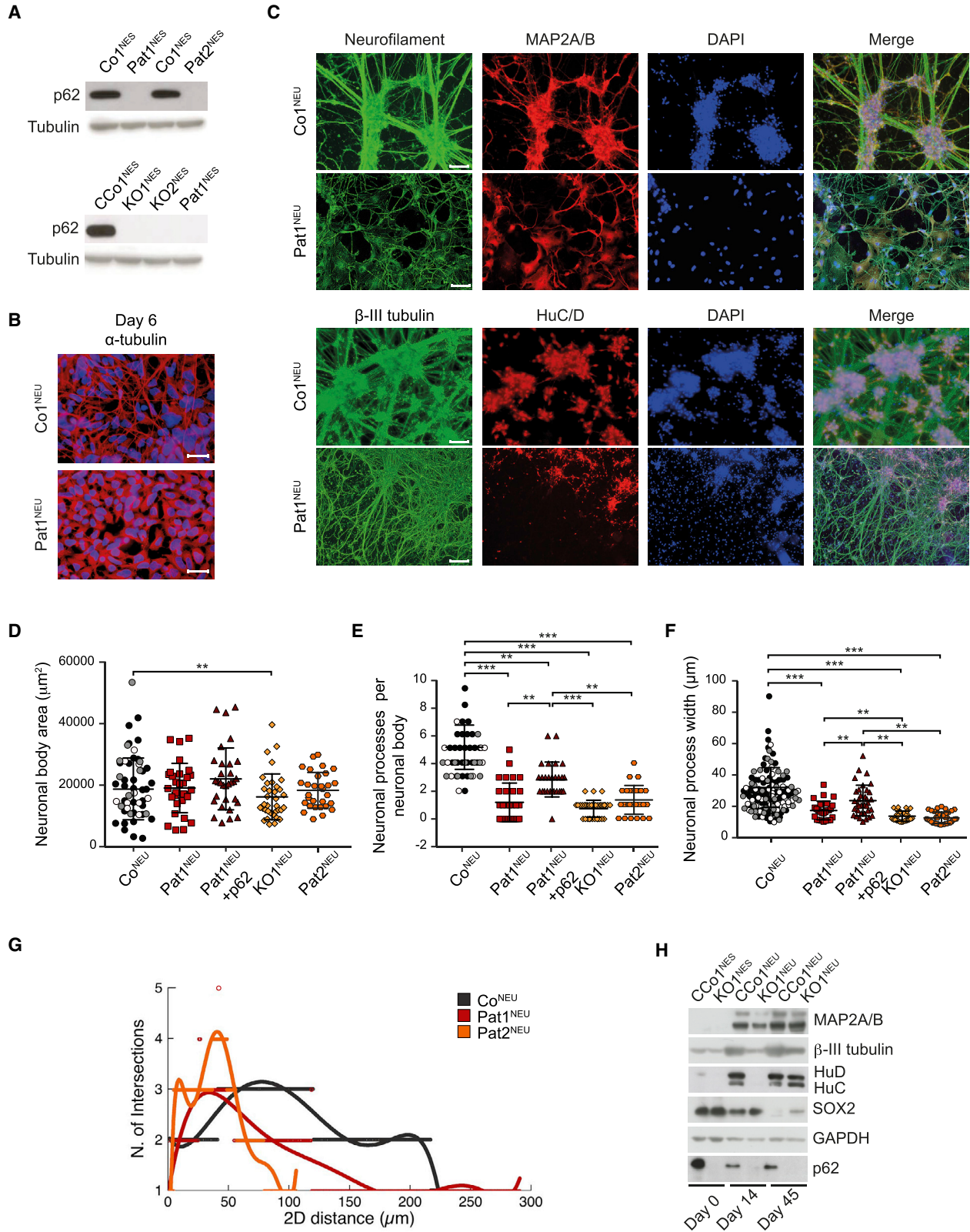
(legend on next page)

lung (Schläfli et al., 2016), liver, kidney, and breast cancers, as well as glioblastoma (Zeng et al., 2014). On the other hand, loss of p62 has also been suggested to promote prostate cancer progression by affecting the tumor's microenvironment (Valencia et al., 2014).

p62, thus, has been suggested to have both pleiotropic and tissue-specific roles, described in often contradictory reports. For instance, together with the E3-ubiquitin ligase PARKIN and the mitochondrial kinase PINK1, p62 has been widely proposed to regulate the maintenance and turnover of mitochondria by selective autophagy, also termed mitophagy (Geisler et al., 2010). Although the phenomenon of mitophagy under certain experimental conditions is generally accepted, its physiological role and mechanism are more controversial (Grenier et al., 2013), and several studies now dispute the involvement of p62 in this process (Narendra et al., 2010; Okatsu et al., 2010). Likewise, p62 has been proposed to stabilize nuclear factor erythroid 2-related factor 2 (NRF2) transcription factor under oxidative stress conditions, by preventing its KEAP1-mediated degradation and thereby triggering an oxidative stress gene expression response (Copple et al., 2010; Fan et al., 2014; Jain et al., 2010; Komatsu et al., 2010; Lau et al., 2010). However, $p62^{-/-}$ mice were still able to activate NRF2-induced gene responses (Kwon et al., 2012) and no changes in NRF2 and KEAP1 were observed in the absence of p62 in a pancreatic tumor model (Valencia et al., 2014).

To understand the disease mechanisms associated with the loss of p62, we studied the cellular and metabolic consequences in neuronal stem cells and neurons, derived from reprogrammed patient fibroblasts, as well as CRISPR/Cas9-targeted neuroepithelial stem cells (NESCs). Our data suggest that p62 is required for normal neurogenesis by controlling the expression of proteins involved in the metabolic shift from aerobic glycolysis to oxidative phosphorylation (OXPHOS) and protecting from oxidative stress. In particular, lactate dehydrogenase A (LDHA), a protein essential for this shift (Zheng et al., 2016), is upregulated and remains high in p62-knockout cells upon neuronal differentiation.

RESULTS

p62 Is Essential for Neuronal Differentiation

In humans, loss of p62 leads to a childhood-onset neurodegenerative disease with no organs affected other than the central nervous system (Haack et al., 2016; Muto et al., 2018). We therefore sought to study the role of p62 and reprogrammed fibroblasts from two patients carrying a nonsense mutation at the 5′ end of SQSTM1 (p.Arg96*, patients II:1 and II:4 from family 4 in Haack et al., 2016) to induced pluripotent stem cells (iPSCs), before differentiating them further to neuroepithelial-like stem cells (Pat1^NES or Pat2^NES) (for details see Experimental Procedures and Falk et al., 2012; Koch et al., 2009). NESCs exhibit an extensive proliferative lifespan and display a high differentiation potential to various neuronal subtypes and glial cells, allowing for a cell-type and patient-specific characterization (Falk et al., 2012; Koch et al., 2009). We confirmed the NESC status of Pat1&2^NES cells by immunofluorescence and western blot of Nestin, SOX2, PLZF, and DACH1 (Figures S1A and S1B). To control for potential effects due to differences in genetic background between Pat1&2^NES cells and control NESCs, we additionally applied CRISPR/Cas9 gene editing technology to control NESCs, targeting the 5′ terminus of SQSTM1, followed by clonal selection. Loss of p62 was confirmed by western blot and qPCR analysis (Figures 1A and S1C). Two clones with confirmed loss of p62 were chosen as p62-knockout (KO) NESCs (KO1^NES and KO2^NES), while two clones that retained normal p62 levels were used as CRISPR control (CCo1^NES and CCo2^NES) cells (see Experimental Procedures for details).

Figure 1. p62 Is Essential for Neuronal Differentiation

(A–C) (A) Representative western blot analysis of p62 in (top) Co1^NES, Pat1^NES, and Pat2^NES cells and (bottom) CCo1^NES, KO1^NES, KO2^NES, and Pat1^NES cells. Tubulin was used as a loading control. n = 3 (n is defined as independent experiments). (B and C) Representative fluorescence images of Co1^NEU and Pat1^NEU after (B) 6 days differentiation, immunostained against α-tubulin (red) and DAPI (blue) (scale bar, 50 μm; n = 5), or (C) 20 days differentiation, immunostained against neurofilament (green), MAP2A/B (red), and DAPI (blue) or against β-III tubulin (green), HuC/D (red), and DAPI (blue) (scale bar, 100 μm; n = 5).

(D–F) Thirty neuronal bodies of Co1^NEU (black), Co2^NEU (white), and Co3^NEU (gray) (pooled under the name Co^NEU); Pat1^NEU (red); Pat1^NEU + p62 (brown); KO1^NEU (yellow); and Pat2^NEU (orange) were analyzed for (D) neuronal body area, (E) number of neuronal processes per neuronal body, and (F) width of neuronal processes. Data are expressed as mean ± SD and differences were tested by a two-tailed t test. ***p < 0.001, **p < 0.01; n = 3.

(G) Linear Sholl analysis representation of 20-days-differentiated control neurons (pooled data from Co1^NEU, Co2^NEU, and Co3^NEU, under the name Co^NEU, dark gray); Pat1^NEU (red); and Pat2^NEU (orange). n = 3. Neuronal processes were analyzed from 15 neuronal bodies per line.

(H) Representative western blot analysis of steady-state levels of MAP2A/B, β-III tubulin, HuC/D, SOX2, and p62 in CCo1^NES and KO1^NES cells undifferentiated and after 14 or 50 days of differentiation. GAPDH was used as a loading control. n = 3.

See also Figures S1 and S2.
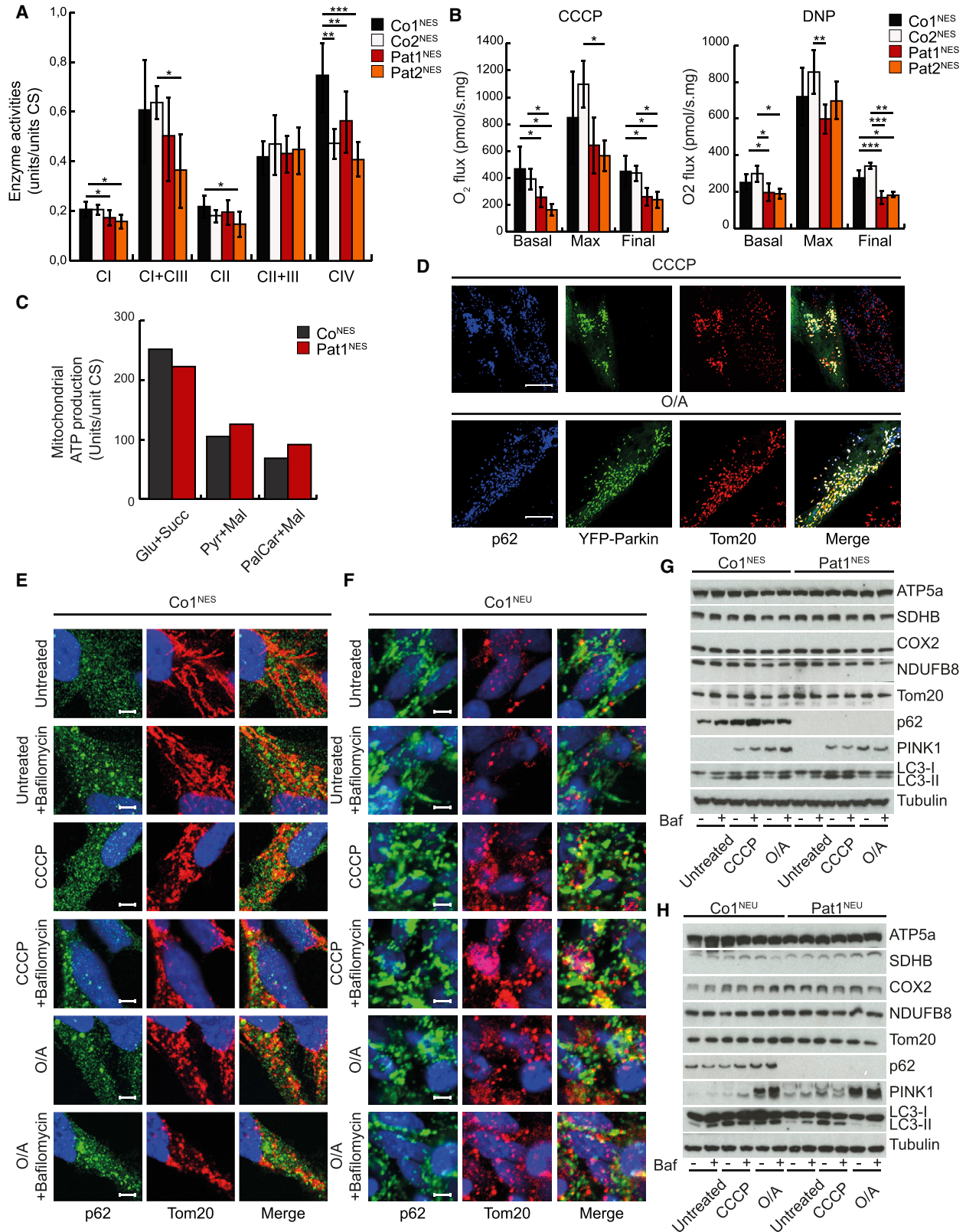
(legend on next page)

Removal of epidermal growth factor and basic fibroblast growth factor from the growth medium induces NESCs to arrest their cell cycle and undergo genomic reprogramming for neuronal differentiation toward neuronal and glial phenotypes. Early steps of this differentiation are marked by the appearance of 1- to 2-μm-thin projections, termed neuronal processes, which will fuse and build a complex network of connected mature neurons with prolonged differentiation. After 6 days of differentiation, control NESCs (Co^{NEU}) presented with the expected formation of neuronal processes, as observed by immunocytochemistry against α-tubulin. In contrast, patient NESCs (Pat1^{NEU}) showed a marked decrease in the formation of these neuronal processes (Figure 1B). After 20 days of differentiation, when morphological maturation of neurons is almost completed, control cells showed a clear organizational structure of thick neuronal processes, while patient-derived neurons showed an aberrant and disorganized morphology along with morphologically undifferentiated cells (Figures 1C and S1D–S1F). Immunostaining, using the neuronal markers Neurofilament, MAP2A/B, HuC/D, and β-III tubulin with subsequent quantification, showed a mild reduction in neuronal body area and a clear reduction in the number and width of mature neuronal processes emerging from these neuronal bodies (Figures 1D–1F). Sholl analysis (Sholl, 1953) demonstrated that patient cells develop interactions within the nearby cell cluster but are unable to connect with more distant cells, having shorter extensions than control cells (Figure 1G) (individual Sholl analyses of the control cells are shown in Figure S1G). This deviant neuronal differentiation could also be observed in CRISPR/Cas9 gene-editing-derived KO^{NES} cells (Figures S2A and S2B), as well as in control NESCs, where p62 expression was silenced by short hairpin RNA

(Figure S2C). Exogenous expression of wild-type p62 in Pat1^{NES} cells reversed this deficiency (Figures 1D–1F and S2D). Western blot analysis of the neuronal markers β-III tubulin, HuC/D, and MAP2A/B, as well as the stem cell marker SOX2, confirmed that, while control cells were able to undergo neuronal differentiation, cells lacking p62 exhibited a general decrease in the expression of neuronal markers and retained a high degree of stemness, even after 45 days of differentiation (Figure 1H). Elevated levels of SOX2 protein in patient neurons after 25 and 45 days of differentiation were confirmed by immunostaining (Figure S2E). Together, our data show that p62 is required for the formation of neuronal processes and the differentiation into neurons.

Loss of p62 in NESCs Results in Reduced Respiratory Chain Function

Mitochondrial function has recently been shown to be required for neuronal differentiation (Khacho et al., 2017), and we therefore compared mitochondrial respiratory chain function of NES control cells and NESCs lacking p62. In agreement with skeletal muscle and fibroblast samples (Haack et al., 2016), Pat1&2^{NES} cells had a mild reduction in respiratory chain enzyme activities of complexes I and IV (Figure 2A), with reduced basal respiration capacity (Figure 2B), but normal mitochondrial ATP production rates (Figure 2C).

An attractive explanation for the reduced respiratory chain function could be a decreased capacity of the cells to remove damaged mitochondria, since p62, together with the E3-ubiquitin ligase PARKIN and the mitochondrial kinase PINK1, has been reported to be important for this process (Park et al., 2014). Human fibroblasts express low levels of endogenous PARKIN and thus, as previously

Figure 2. Loss of p62 in NESCs Results in Reduced Respiratory Chain Function, but p62 Is Dispensable for Mitophagy
(A) Mitochondrial respiratory chain enzyme activities in Co1^{NES} (black), Co2^{NES} (white), Pat1^{NES} (red), and Pat2^{NES} (orange). Complex I (CI; NADH coenzyme Q reductase), complex I + III (CI+III; NADH cytochrome *c* reductase), complex II (CII; succinate dehydrogenase), complex II + III (CII+III; succinate cytochrome *c* reductase), and complex IV (CIV; cytochrome *c* oxidase) are shown. Data are presented as mean ± SD and differences were tested by a two-tailed t -test. *$p < 0.05$, **$p < 0.01$, ***$p < 0.001$, n = 3.
(B) Oxygen consumption rates from Co1^{NES} (black), Co2^{NES} (white), Pat1^{NES} (red), and Pat2^{NES} (orange), treated with CCCP or dinitrophenol (DNP). Data are expressed as mean ± SD and differences were tested by a two-tailed t test. *$p < 0.05$, **$p < 0.01$, ***$p < 0.001$, n = 3.
(C) Mitochondrial ATP production rates in Co1^{NES} (gray) and Pat1^{NES} (red) supplemented with glutamate/succinate (Glu+Succ), pyruvate/ L-malate (Pyr+Mal), or palmitoylcarnitine/L-malate (PalCar+Mal). Data are expressed as units per unit of citrate synthase (CS).
(D) Representative confocal images of control fibroblasts transfected with YFP-Parkin (green) and treated with CCCP (20 μM) (top) or O/A (10 μM/1 μM) (bottom) for 2 h. Fibroblasts were immunostained against Tom20 (red) and p62 (blue). n = 3.
(E) Representative confocal images of Co1^{NES} cells treated for 2 h with or without 10 μM CCCP or O/A (5 μM/1 μM) and with or without 50 nM bafilomycin, using antibodies against p62 (green) and TOM20 (red) and DAPI stain (blue). Scale bar: 20 μm. n = 3.
(F) Representative confocal images of 14-days-differentiated neurons treated for 2 h with or without 10 μM CCCP or O/A (5 μM/1 μM) and with or without 50 nM bafilomycin, using antibodies against p62 (green) and TOM20 (red) and DAPI staining (blue). Scale bar: 20 μm. n = 3.
(G and H) Representative western blot analysis of (G) Co1^{NES} and Pat1^{NES} cells treated for 12 h or (H) Co1^{NEU} and Pat1^{NEU} after 20 days of differentiation treated for 2 h with or without 10 μM CCCP or O/A (5 μM/1 μM) and with or without 50 nM bafilomycin for 2 h. n = 3.
See also Figures S2–S4 and Table S2 for p62 primers.
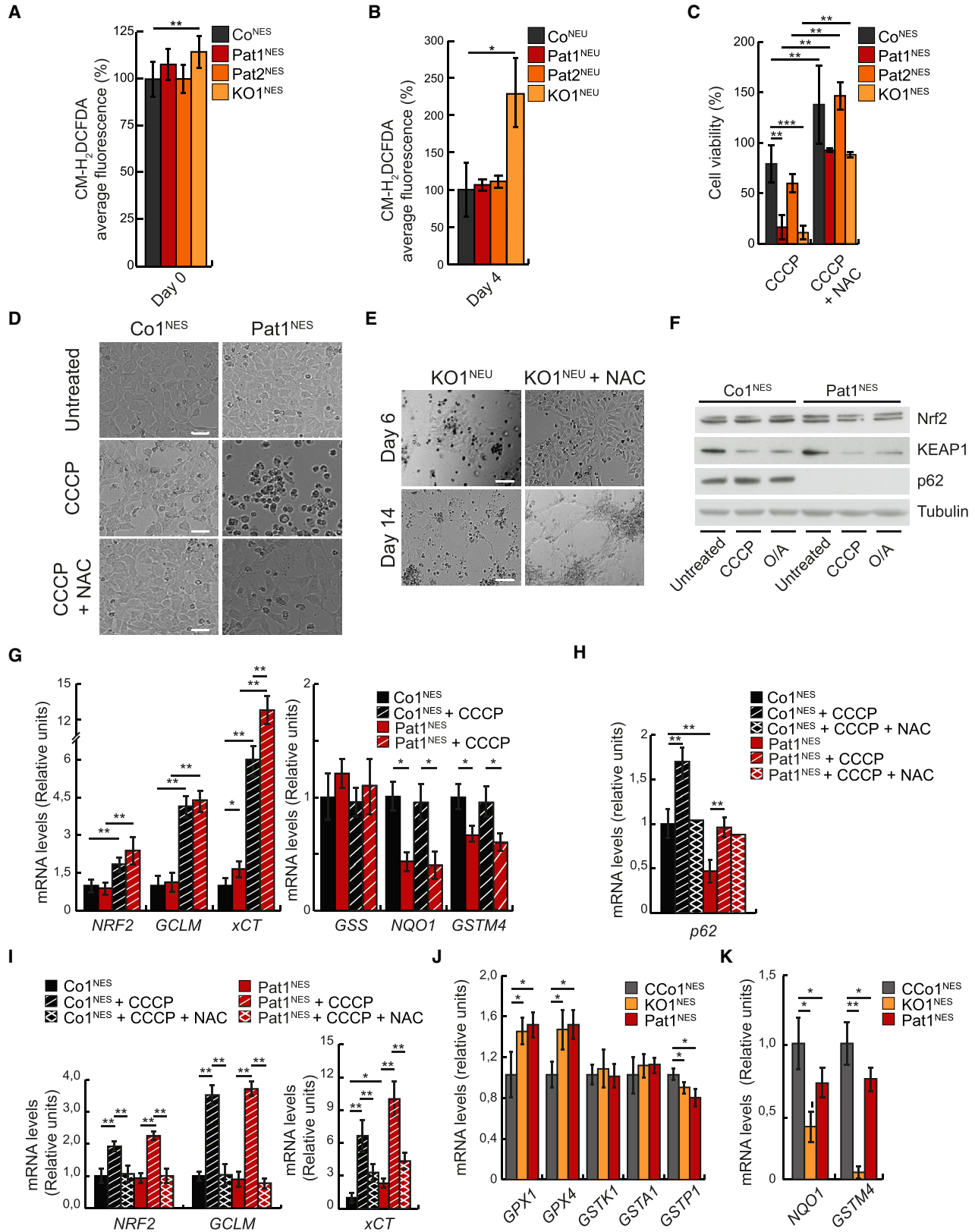
(legend on next page)

shown, only the exogenous overexpression of YFP-PARKIN showed the typical co-localization between the mitochondrial outer membrane protein TOM20 and p62 upon treatment with the mitochondrial uncoupler carbonyl cyanide m-chlorophenyl hydrazone (CCCP) or with the mitochondrial complex inhibitors oligomycin and antimycin (O/A) (Figures 2D, S2F, and S2G). In contrast, both NESCs and NESCs undergoing neuronal differentiation (14-day neurons) express high levels of endogenous PARKIN and the absence of p62 should therefore have an impact on mitochondrial clearance upon depolarization (Figure S2H). However, both cell types showed very little co-localization of p62 with TOM20 with or without the addition of bafilomycin, an inhibitor of the lysosomal proton pump that blocks lysosomal function (Figures 2E, 2F, and S2G). Furthermore, fibroblasts (Figure S2I), NESCs (Figure 2G), and differentiated neurons (Figure 2H) lacking p62 showed the expected LC3II and PINK1 levels upon CCCP or O/A treatment, suggesting that autophagosome formation and PINK1 stabilization, two classical features of mitophagy, were activated even in the absence of p62. Induction of mitophagy by mitochondrial toxins is associated with the loss of mitochondrial markers (Narendra et al., 2012); however, we observed only a mild reduction of mitochondrial proteins in control and patient fibroblasts, which could be reversed with bafilomycin (Figures S2J and S2K), and no reduction in NESCs (Figure 2G) and neurons (Figure 2H). Co-localization of the autophagosomal marker LC3II or lysosomal marker LAMP2 with the mitochondrial marker TOM20 was not affected in fibroblasts (Figures S2L and S2M), NESCs (Figures S3A and S3B), or differentiated neurons (Figures S4A and S3B) upon loss of p62. Together, these results demonstrate that p62 is not required for the autophagocytic removal of mitochondria upon mitochondrial depolarization in cells with endogenous expression of PARKIN. It also suggests that the observed neuronal phenotypes caused by the loss of p62 are not associated with deficient mitophagy.

Compromised Neuronal Differentiation Can Be Partly Rescued by N-Acetyl-L-cysteine

Oxidative stress and the regulation of reactive oxygen species (ROS) levels have previously been shown to have an important role during neuronal differentiation (Vieira et al., 2011). Mitochondria are the main source of intracellular ROS and a mild mitochondrial defect can lead to increased levels of ROS. Moreover, p62 has been suggested to regulate NRF2, previously shown to regulate genes containing antioxidant response elements (AREs) via KEAP1 (Jiang et al., 2015). KEAP1 degrades NRF2 and thus the loss of p62 would deregulate the KEAP1-NRF2-ARE pathway (Komatsu et al., 2010) and increase sensitivity to oxidative stress (Park et al., 2015). Although patient NESCs undergoing neuronal differentiation did not have increased ROS levels, $KO1^{NEU}$ cells showed a marked increase after 4 days differentiation (Figures 3A and 3B), consistent with the more severe phenotype. In addition, glutathione levels were reduced in the absence of p62 (Figure S4C). Furthermore, NESCs lacking p62 were more sensitive to CCCP treatment in comparison with control cells (Figure 3C). Supplementing growth conditions with the antioxidant N-acetyl-L-cysteine (NAC) allowed p62-deficient NESCs to partially regain their differentiation potential, as indicated by reduced cell death (Figures 3C and 3D) as well as increased axonal projections (Figure 3E), suggesting an important role of p62 in the cellular oxidative stress

Figure 3. Compromised Neuronal Differentiation due to Deficient p62 Can Be Rescued by NAC

(A) Quantification of the average CM-H_2DCFDA signal in four control NESCs (Co1^{NEU}, Co2^{NEU}, Co3^{NEU}, CCo1^{NEU} [pooled as Co^{NEU}]), Pat1^{NES}, Pat2^{NES}, and KO1^{NES}.

(B) As in (A), but on cells after 4 days of differentiation. Data are expressed as mean ± SD and differences were tested by a two-tailed t test. *p < 0.05, **p < 0.01; n = 3 with 50 cells analyzed per experiment.

(C) Cell viability assay of CCo1^{NES}, Co1^{NES}, Co2^{NES}, and Co3^{NES} (dark gray, pooled as Co^{NES}), Pat1^{NES} (red), and Pat2^{NES} (orange) after a 15-h treatment with 20 μM CCCP or 20 μM CCCP and 1 mM NAC as indicated. Data are presented as mean ± SD and differences were tested by a two-tailed t test. **p < 0.01 and ***p < 0.001, n = 3.

(D) Representative bright-field images of Co1^{NES} and Pat1^{NES} cells, treated for 15 h with 20 μM CCCP or 20 μM CCCP +1 mM NAC. Scale bar, 100 μm; n = 3.

(E) Representative bright-field images of KO1^{NES} (±1 mM NAC) subjected to differentiation for 6 or 14 days. Scale bar, 100 μm; n = 3.

(F) Representative western blot analysis of Nrf2, KEAP1, and p62 in Co1^{NES} and Pat1^{NES} cells untreated and treated for 12 h with 10 μM CCCP or 10 μM oligomycin and 1 μM antimycin (O/A) as indicated. Tubulin was used as a loading control. n = 3.

(G–I) qRT-PCR analysis in Co1^{NES} (black) and Pat1^{NES} (red) cells, treated (striped) or untreated (solid) for 6 h with 10 μM CCCP and/or 1 mM NAC as indicated for (G) NRF2, GCLM, and xCT (left) and GSS, NQO1, and GSTM4 (right) (n = 4); (H) p62 (n = 3); or (I) NRF2, GCLM, and xCT (n = 3). β-actin was used as an endogenous control. Data are expressed as mean ± SD and differences were tested by a two-tailed t test. *p < 0.05 and **p < 0.01.

(J and K) qRT-PCR analysis of CCo1^{NES} (gray), KO1^{NES} (yellow), and Pat1^{NES} (red) cells for (J) GPX1, GPX4, GSTK1, GSTA1, and GSTP1 or (K) NQO1 and GSTM4 steady-state levels. β-actin was used as an endogenous control. Data are expressed as mean ± SD and differences were tested by a two-tailed t test. *p < 0.05, **p < 0.01, n = 3. See also Figure S4 and Table S2 for primers used.
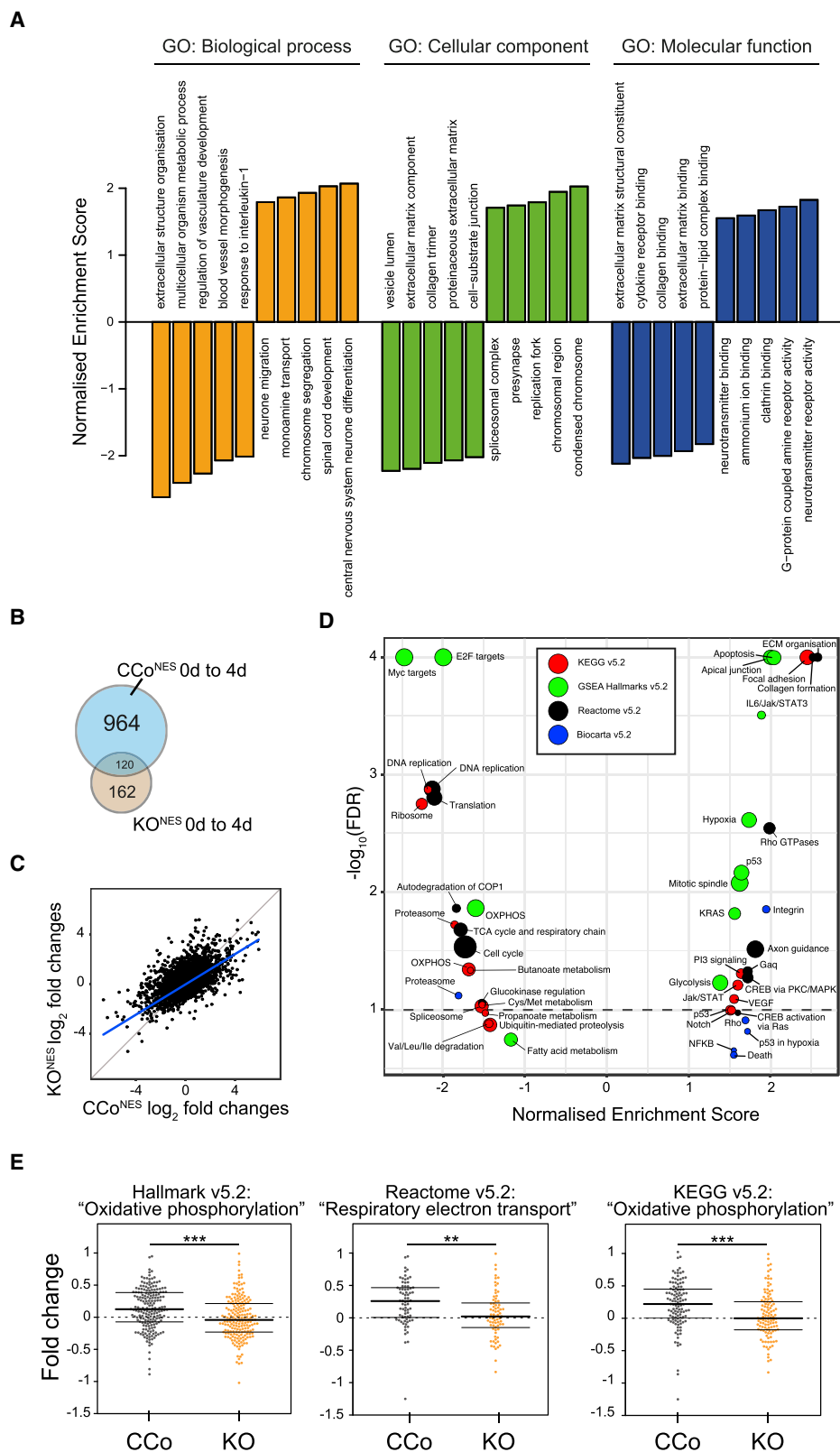
(legend on next page)

response. However, we observed no differential response between control cells and cells lacking p62 treated with CCCP in KEAP1 levels (Figure 3F) and antioxidant genes *NRF2*, γ-glutamylcysteine synthetase (*GCLM*), and the calcium channel blocker resistance protein (*CCBRP*, also known as *xCT* or *SLC7A11*) (Figures 3G and S4D). Interestingly, p62 protein, mRNA expression levels, and subcellular redistribution to a more punctuated pattern increased in control cells after CCCP and O/A treatment (Figures 2G, 3H, and S4E), suggesting a role of p62 in the antioxidant response. Accordingly, NAC treatment prevented the increase of the antioxidant genes *xCT*, *NRF2*, *GCLM*, and *p62* (Figures 3H and 3I). In agreement with increased oxidative stress, several key mitochondrial antioxidant enzymes, such as *GPX1*, *GPX4*, *NQO1*, *GSTM4*, and *GSTP1*, were differentially expressed in cells lacking p62 (Figures 3J, 3K, S4F, and S4G), supporting the notion that p62 is essential in protecting neuronal progenitor cells from oxidative damage, independent of the KEAP1-NRF2-ARE pathway.

p62 Regulates Gene Expression Changes Involved in the Metabolic Switch Occurring during Neuronal Differentiation

To identify additional pathways affected by the absence of p62, we studied changes in the global gene expression patterns of NESCs during 4 days of differentiation in the presence or absence of p62. To ensure equal genetic background and stemness status of the NESCs prior to differentiation, we chose to use CRISPR/Cas9-derived KO (KO^{NES}) and control (CCo^{NES}) cells. Neuronal development is associated with changes in the expression of several neuronal markers, and as expected, the neuronal markers Pax6, NeuroG1, NeuroD1, and NeuroD2 were upregulated in control cells 4 days after the induction of neuronal differentiation (Table S1). Furthermore, we used WebGestalt to perform gene set enrichment analysis (GSEA) to cluster genes according to gene ontology terms related to biological function, molecular process, or cellular component (Wang et al., 2013). Transcriptomic data revealed a positive enrichment of "central nervous system neuron differentiation" and "neurotransmitter receptor activity" (Figure 4A).

A comparison of the 500 most significant genes against the Human Gene Atlas with EnrichR presented fetal brain as the tissue with the most similar gene expression profile (q = 0.002). These data indicate that our neuronal differentiation model indeed represents stages of neuronal development.

Comparison of differential expression patterns during 4 days of NESC differentiation between p62-KO and control cells identified 964 and 162 unique differentially expressed genes in CCo^{NES} or KO^{NES} cells at α = 0.01, respectively (Figures 4B and 4C, Table S1). The expression changes of 120 genes were common between the two genotypes, suggesting that these genes are not related to p62 function. KO^{NES} cells had a milder gene response to differentiation, with genes associated with neuronal differentiation induced only in control NESCs (Table S1), corroborating the neuronal differentiation defect observed due to the absence of p62. A pathway-based GSEA revealed a positive enrichment for apoptotic pathways, which is an imprint of increased death of KO^{NES} cells under differentiation (Figure 4D). Recent work from Zheng and colleagues suggests that neuronal progenitor cells initiate a metabolic shift from glycolytic to a more OXPHOS metabolism during differentiation (Zheng et al., 2016). In agreement, OXPHOS-related genes increased in control NESCs undergoing differentiation (Figure 4E). However, KO^{NES} cells had a significantly lower expression of OXPHOS genes, with a median log2-fold change around 0, thus showing that the loss of p62 prevents NESCs from reprogramming their energy metabolism (Figure 4E).

Loss of p62 Alters Cellular Energy Metabolism

We argued that the loss of p62 altered the intracellular environment already in NESCs, preventing them from fully committing to neuronal differentiation. We therefore compared transcriptomic (Figure 5A) and proteomic (Figure 5B) expression profiles of NESCs lacking p62 with those of control NESCs before differentiation. We found 695 differentially expressed transcripts (5.1% of all accepted transcripts) and 168 differentially expressed proteins (5.5%) at a false discovery rate of <0.05 (Figures 5A and

Figure 4. p62 Is Essential for the Metabolic Switch Required during Neuronal Differentiation
(A) Gene ontology (GO) analysis comparing gene expression profiles of CCo1^{NES} and CCo2^{NES} cells after 0 and 4 days of differentiation.
(B) Transcriptomic profiling of CCo1^{NES}, CCo2^{NES}, KO1^{NES}, and KO2^{NES} cells during differentiation. Venn diagram showing the number of significantly differentially expressed genes at p < 0.01 in CCo1^{NES}, CCo2^{NES}, KO1^{NES}, and KO2^{NES} cells during differentiation.
(C) Log2-fold changes of transcripts during differentiation of control CCo1^{NES} and CCo2^{NES} cells against KO1^{NES} and KO2^{NES} cells. In blue is the fitted regression line of a linear model, in gray the 45° line.
(D) Gene set enrichment analysis of RNA sequencing data against four different databases. The dotted line indicates a false discovery rate (FDR) of 0.01.
(E) Comparison of gene expression fold changes of OXPHOS-related gene sets, annotated in three databases, in CCo and KO cells after 4 days differentiation. **p < 0.01, ***p < 0.001, calculated using Welch's t test. Boxplot outlines depict lower and upper quartile and median. See also Figure S5 and Table S1.
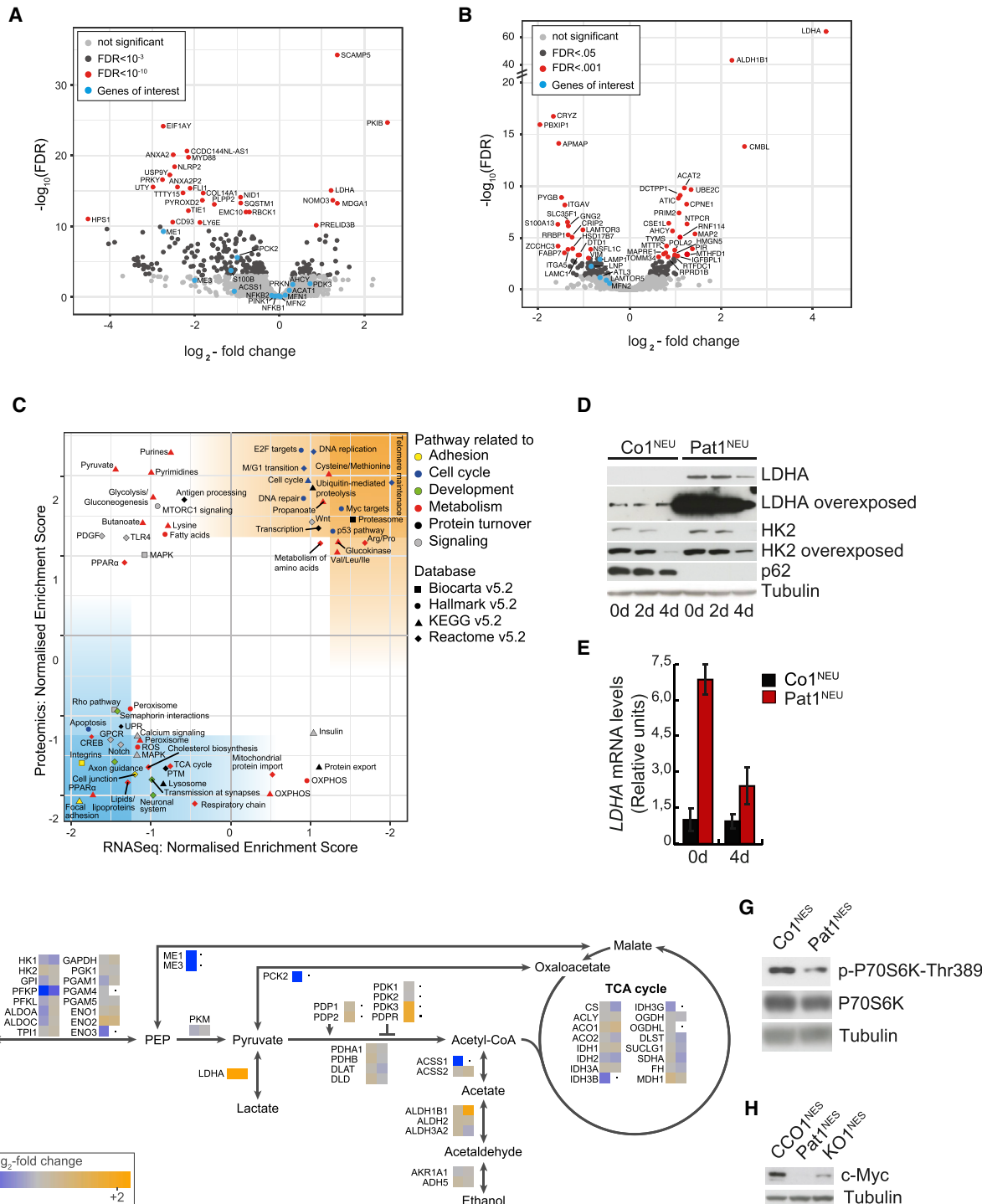
Figure 5. Loss of p62 Alters Cellular Energy Metabolism

(A) High-throughput data analysis of CCo1^{NES}, CCo2^{NES}, KO1^{NES}, and KO2^{NES} cells before differentiation. Volcano plot of differentially transcribed genes, identified by RNA sequencing (n = 13,601 after filtering). FDR, false discovery rate.

(B) Volcano plot of differentially expressed proteins identified by proteomics (n = 3,058 after filtering).

(C) Gene set enrichment analysis of RNA sequencing data against proteomics analysis. Blue- and orange-colored areas indicate increasing confidence.

5B and Table S1). One of the most significant changes observed due to the loss of p62 was the profound upregulation of LDHA, an enzyme that catalyzes the conversion between pyruvate and lactate, in both the transcriptomic and the proteomic datasets (Figures 5A and 5B). We confirmed that this upregulation was a consequence of the loss of p62, as patient and KO cell lines showed the same response by western blotting (Figure S5A) and qRT-PCR (Figure S5B). Interestingly, LDHA levels did not change in control NESCs after 4 days differentiation, while they slightly decreased in the absence of p62, on both protein and transcript levels (Figures 5D and 5E). To our surprise, though, fibroblasts obtained from both patients who were the initial source for the generation of the Pat1 and Pat2 NESCs did not show this increase (Figure S5C), suggesting that this LDHA induction is a tissue-specific response. GSEA against four different pathway libraries further revealed that loss of p62 leads to increased expression of several gene groups involved in pyruvate metabolism and pyruvate dehydrogenase (PDH) regulation (Figures 5A–5C). For instance, the PDH complex was negatively regulated via its inhibitor PDH kinase 3 (PDK3), while the PDH phosphorylase (PDP) was inhibited via the PDP regulatory subunit (PDPR). In addition, gluconeogenesis and fatty acid biosynthesis were downregulated, as reflected by the transcript levels of phosphoenolpyruvate carboxykinase 2 (PCK2) and malic enzymes (ME) 1 and 3, respectively (Figure 5F). Amino acid metabolic pathways appeared upregulated in the absence of p62, probably as a consequence of a dysregulation in pyruvate metabolism (Figure 5C).

LDHA is a key regulator of anaerobic metabolism and its expression is regulated by the Phosphatidylinositol 3-kinase/Akt/Mammalian target of rapamycin (PI3K/Akt/mTOR) pathway, among others (Valvona et al., 2016; Woo et al., 2015). Previous work suggests that p62 regulates mTORC1 pathway activation (Duran et al., 2011), leading to the stabilization of the v-Myc avian myelocytomatosis viral oncogene homolog (c-Myc), an important transcription factor involved in cell cycle progression, apoptosis, cellular transformation, cancer progression (Valencia et al., 2014), and neuronal differentiation

(Iavarone and Lasorella, 2014). In agreement, loss of p62 resulted in reduced mTOR activation, as indicated by phosphorylation of Thr389 of P70S6K (Figure 5G), and reduced expression of the LAMTOR proteins LAMTOR1, LAMTOR3, and LAMTOR5 (Figures 5B and 5C). As expected, c-Myc protein levels were reduced in the absence of p62, suggesting reduced mTOR activation (Figure 5H). In stark contrast, transcripts of c-Myc targets, such as genes associated with glucose metabolism (*LDHA*), DNA replication (*MCM2*, *MCM6*), or proteasomal function (*PSMA4*, *PSMA7*), were upregulated (Figures 5A–5C), indicating differential gene regulation of c-Myc targets upon loss of p62. Interestingly, the pro-glycolytic modulator hexokinase 2 (HK2) was elevated in NESCs lacking p62, and only slightly reduced during 4 days of differentiation, while it was completely downregulated in control cells (Figure 5D and Table S1), further supporting the notion of a dysregulated energy metabolism.

Physiological Oxygen Concentrations Reveal a Pro-glycolytic Metabolism in the Absence of p62

As described, the increased levels of LDHA could not be explained by c-Myc activation. Exposing mice or cultured cells to oxygen concentrations lower than normoxia (20% oxygen concentration) triggers the activation of anaerobic glycolysis and diminishes mitochondrial aerobic metabolism (Jain et al., 2016). Moreover, transcription of LDHA and other glycolytic genes is activated by Hif-1α under hypoxic conditions (Cui et al., 2017). Results in cancer cells exposed to strict hypoxia (≤1% oxygen concentration) showed hypoxia-activated macroautophagic removal of p62 (Pursiheimo et al., 2009) and p62 regulation of PHD3 activity (Rantanen et al., 2013). Compared with controls, KO1&2^NES presented higher levels of LDHA, HK2, and PDK3, a typical pro-glycolytic gene expression profile, already in normoxia, and we therefore hypothesized that p62-deficient NESCs assume a constant hypoxic state when cultured in normoxia. Exposure to physiological oxygen levels would then even further aggravate the abnormal gene expression profile. The exact *in vivo* oxygen pressure of a tissue is difficult to determine, and we decided

---

(D) Representative western blot analysis of LDHA and HK2 in Co1^NEU and Pat1^NEU after 0, 2, or 4 days of differentiation. Tubulin was used as a loading control. n = 3.

(E) qRT-PCR analysis of *LDHA* steady-state levels in Co1^NEU (dark gray) and Pat1^NEU (red) cells after 0 or 4 days of differentiation. β-actin was used as an endogenous control. n = 3.

(F) Expression levels of enzymes involved in pyruvate metabolism in undifferentiated KO1&2^NES cells compared with undifferentiated CCo1&2^NES cells. Left square of mini-heatmaps, transcriptome; right square, proteome; black dot, data not captured.

(G) Representative western blot analysis of Thr389 phosphorylation of P706SK in Co1^NES and Pat1^NES cells. Tubulin was used as a loading control. n = 3.

(H) Representative western blot analysis of Myc steady-state levels in CCo1^NES, Pat1^NES, and KO1^NES cells. Tubulin was used as a loading control. n = 3.

See also Figure S5 and Table S2 for LDHA primers.

A

Co1^{NES} Pat1^{NES}

Hif1-α
Hif1-α overexposed
p62
Tubulin

0h 8h 24h   0h 8h 24h   **3% O$_2$**

B

Hif-1α levels (relative units)

160
120
80
60
40
0

■ Co1^{NES}
■ Pat1^{NES}

8h 24h   8h 24h

**

***

C

Co1^{NES} Pat1^{NES}

HK2
PDK1
PDK3
LDHA
LDHA overexposed
Tubulin

0h 8h 24h   0h 8h 24h   **3% O$_2$**

D

Untreated   5h CoCl$_2$ 24h CoCl$_2$

Hif1-α
Tubulin

Co1^{NES} Pat1^{NES} Co1^{NES} Pat1^{NES} Co1^{NES} Pat1^{NES} **200 μM CoCl$_2$**
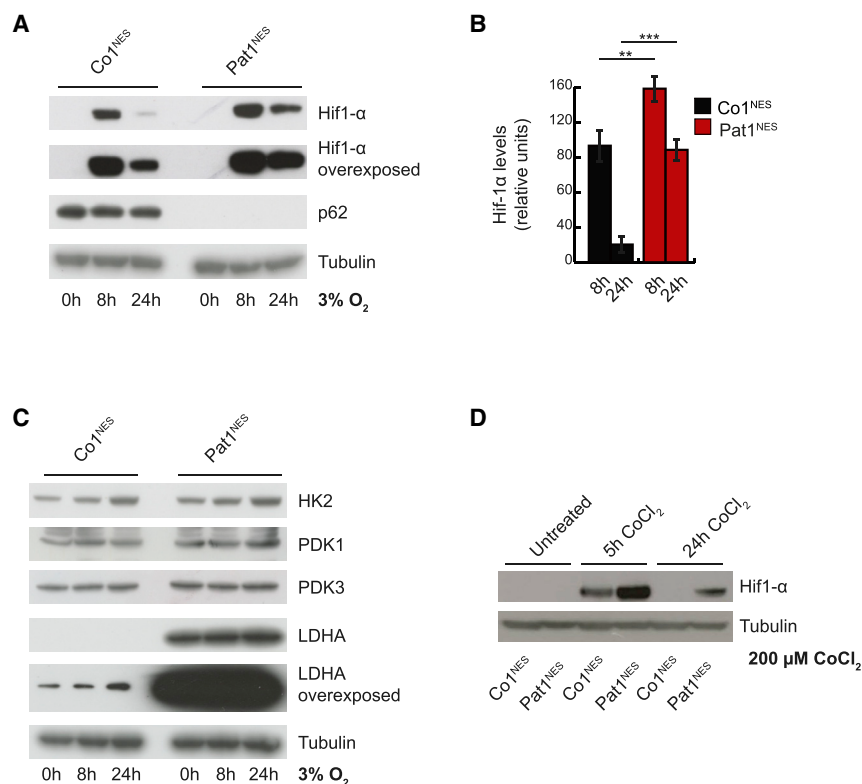
Figure 6. Physiological Oxygen Concentrations Reveal a Pro-glycolytic Metabolism in the Absence of p62

(A) Representative western blot analysis of Hif-1α and p62 steady-state levels in Co1^{NES} and Pat1^{NES} cells, cultured for 0, 8, or 24 h at 3% O$_2$. Tubulin was used as a loading control (n = 3).

(B) Quantification of (A). Data are expressed as mean ± SD and differences were tested by a two-tailed t test. **$p < 0.01$, ***$p < 0.001$, n = 3.

(C) Western blot analysis of HK2, PDK1, PDK3, and LDHA as in (A). Tubulin was used as a loading control. n = 3.

(D) Western blot analysis of Hif-1α expression in Co1^{NES} and Pat1^{NES} cells, cultured for 0, 5, or 24 h in the presence of 200 μM CoCl$_2$. Tubulin was used as loading control. n = 5. See also Figure S6.

to incubate NESCs at 3% oxygen concentration. As previously reported (López-Hernández et al., 2012), Hif-1α expression was low and almost undetectable in control cells in normoxia, but increased profoundly after several hours in hypoxia, before decreasing again after 24 h (Figures 6A, 6B, S6A, and S6B). Hif-1α levels also responded to low oxygen concentrations in NESCs lacking p62 and even remained elevated after 24 h, compared with control NESCs (Figures 6A, 6B, S6A, and S6B). As expected, other factors, such as HK2, PDK1, and PDK3, also had a mild induction under these conditions, while LDHA levels remained increased in patient NESCs (Figures 6C and S6C). We confirmed the induction of Hif-1α by treating NESCs with CoCl$_2$, known to mimic hypoxia (López-Hernández et al., 2015), demonstrating that even in the absence of p62, NESCs responded to hypoxic conditions (Figures 6D and S6D), suggesting that the pronounced pro-glycolytic profile observed in these cells is independent of Hif-1α.

DISCUSSION

More than 130 million people are predicted to suffer from some form of dementia by 2050. With an increasing aging population, neurodegenerative disorders have already become a major burden, not only to the affected. Given

the urgency of understanding these diseases, surprisingly few treatment options are available. The importance of particular metabolic networks is increasingly being recognized in disease progression, but studying their interplay has been more difficult. We decided to investigate the molecular consequences of a monogenic neurodegenerative disorder in a brain-appropriate model. The autophagy adaptor protein SQSTM1/p62 has been associated with a number of different functions, including as adaptor for mitochondrial clearance. This association stems from observations made in immortalized cell lines, exogenously overexpressing several components of the proposed process, such as PARKIN or LC3 (Park et al., 2014). We could not confirm this commonly assumed association between p62 and mitophagy in NESCs or neurons, which naturally express high levels of PARKIN.

In contrast, our data indicate that p62 is required for neuronal progenitor cells to change their metabolic microenvironment to a more oxidative metabolism, necessary for neurodifferentiation. Neuronal development is a metabolically dynamic process, during which the interconnection between aerobic glycolysis and OXPHOS is crucial for proper differentiation (Agostini et al., 2016). We observed that the loss of p62 resulted in a significant upregulation of the glycolytic regulators LDHA and HK2 and the inability to promote OXPHOS gene expression.

Downregulation of LDHA and HK2 is essential during neuronal differentiation and is blocked by exogenous expression of LDHA (Zheng et al., 2016). Induction of differentiation did lead to the expected decrease in LDHA and HK2 levels in the absence of p62, but levels remained high, suggesting that the initial levels were too high and/or that p62 is involved in their turnover. The consequences, however, are that although the cell is initiating some of the required steps for differentiation, the metabolic environment prevents their execution. Support comes from a recent observation of increased lactate in the ventricular cerebrospinal fluid of a patient with disrupted p62 (Muto et al., 2018). Interestingly, the same study also disrupted p62 expression in a zebrafish model, and reported structural defects in the cerebellum, including reduced axonal connections and complete atrophy. These observations strongly support our observation that p62 is important for correct neuronal function. Several regulators of LDHA have been reported, including c-Myc and Hif-1α (Valvona et al., 2016), and numerous c-Myc targets were upregulated in the absence of p62, including LDHA, but c-Myc itself was downregulated, on both mRNA and protein levels, suggesting alternative transcriptional regulatory mechanisms of its targets. Hif-1α is recognized as the key regulator of systemic and cellular responses to low oxygen concentrations, and p62-KO cells grown under physiological oxygen levels revealed a pronounced Hif-1α stabilization, as well as increased expression of pro-glycolytic genes, such as *LDHA*, *HK2*, *PDK1*, or *PDK3*. However, in normoxia, where Hif-1α levels are similar, NESCs lacking p62 already present with increased LDHA levels, suggesting that p62 is required for Hif-1α-dependent downregulation during hypoxia but that another factor(s) must be involved in the upregulation of LDHA. Interestingly, fibroblasts from p62$^{-/-}$ patients did not have increased LDHA levels. Recently, two oxygen-sensing cysteine residues in p62 were reported to be important during a p62-dependent autophagic stress response (Carroll et al., 2018), thus suggesting that p62 itself might have oxygen-sensing capacity. Our results indicate that under reduced oxidative stress, either due to reduced oxygen pressure or due to supplementation of antioxidant, neurodifferentiation is improved. Thus, p62 is important during certain stages of development or under stress conditions, which could explain both the normal neuronal development until childhood and the progressive nature of clinical presentation of patients with disrupted p62 (Haack et al., 2016; Muto et al., 2018).

Although mature neurons are thought to primarily rely on OXPHOS for ATP synthesis (Tavernarakis and Palikaras, 2012), a more glycolytic energy metabolism in the brain has been proposed during childhood (Goyal et al., 2014). Such a shift in preference could explain the timing of disease onset and the progressive nature of the clinical presentations in the patients with mutations in p62 (Haack et al., 2016; Muto et al., 2018). The appearance of p62-positive aggregates in Purkinje cells in the cerebellum of old mice also points to an important role of p62 in the brain (Carroll et al., 2018). Increased demands on respiration could also increase oxidative stress, and NESCs lacking p62 displayed increased ROS formation during maximal respiration and differentiation, with several antioxidant pathways induced, including GPX1, GPX4, or ALDH1B1 and decreased levels of NQO1. Alterations in the cellular antioxidant response are in agreement with observations made in p62$^{-/-}$ mice, which also showed reduced NQO1 levels and altered GSH/GSSG ratio (Kwon et al., 2012). Interestingly, NQO1$^{-/-}$ mice showed an unbalanced redox status and accumulation of lactate and decreased glucose levels, suggesting a link between low NQO1 levels and glucose metabolism (Gaikwad et al., 2001). NRF2 is a key regulator of the antioxidant response and the KIR domain of p62 is thought to interact with the NRF2 regulator KEAP1. However, we found no dysfunctional KEAP1-NRF2-ARE pathway regulation upon deletion of p62 in NESCs, which is in agreement with results both in p62$^{-/-}$ mice (Kwon et al., 2012) and in pancreatic tumor cells (Valencia et al., 2014).

p62-KO mice are viable (Durán et al., 2004; Kwon et al., 2012), but die prematurely (Kwon et al., 2012) and present with several neurological phenotypes, ranging from memory loss to behavioral abnormalities to the accumulation of Tau tangles (Ramesh Babu et al., 2008). The patients reported by us also had memory loss and elevated Tau levels (Haack et al., 2016), demonstrating the similarities of the two systems. In addition, p62 was shown to be important for neuronal cell survival and development in rats (Joung et al., 2005). However, p62 ablation rescues the neural stem cell pool in the subventricular zone and dental gyrus of FIP 200-KO mice at p28, suggesting the importance of p62 in the regulation of neuronal development (Wang et al., 2016).

A carefully regulated metabolic environment is increasingly recognized as an important part of neuronal brain development (Agostini et al., 2016; Herrero-Mendez et al., 2009; Schönfeld and Reiser, 2017; Sonntag et al., 2017), and our data clearly show that p62 is required for the metabolic transition during neuronal differentiation.

In conclusion, our findings shed light on the pathogenetic mechanisms behind the childhood onset of ataxia, dystonia, and cognitive decline that result from loss of p62. Importantly, they also indicate that an active promotion of a metabolic shift from glycolysis to OXPHOS is required for neuronal survival beyond the early stages of brain development, and that an inability to promote this shift can lead to neurodegeneration.

EXPERIMENTAL PROCEDURES

Detailed descriptions of experimental procedures can be found in the Supplemental Information.

Ethical Considerations

This study has been approved by the Regional Ethics Committee at Karolinska Institutet in Stockholm, Sweden. Informed consent was obtained from all individuals involved.

Cell Culture

Human primary skin fibroblasts were reprogrammed to iPSCs and subsequently induced to NESCs as described in detail in Supplemental Experimental Procedures.

CRiSPR/Cas9 Gene Editing

Generation of p62-KO cell lines was performed as described in detail in Supplemental Experimental Procedures.

Transcriptomic and Proteomic Analysis

Samples were prepared and analyzed as described in detail in Supplemental Experimental Procedures.

CONTACT FOR DETAILS AND RESOURCE SHARING

Further information and requests for resources and reagents should be directed to Anna Wredenberg (anna.wredenberg@ki.se).

SUPPLEMENTAL INFORMATION

Supplemental Information includes Supplemental Experimental Procedures, six figures, two tables, and one data file and can be found with this article online at https://doi.org/10.1016/j.stemcr.2019.01.023.

REFERENCES

Agostini, M., Romeo, F., Inoue, S., Niklison-Chirou, M.V., Elia, A.J., Dinsdale, D., Morone, N., Knight, R.A., Mak, T.W., and Melino, G. (2016). Metabolic reprogramming during neuronal differentiation. Cell Death Differ. 23, 1502–1514.

Carroll, B., Otten, E.G., Manni, D., Stefanatos, R., Menzies, F.M., Smith, G.R., Jurk, D., Kenneth, N., Wilkinson, S., Passos, J.F., et al. (2018). Oxidation of SQSTM1/p62 mediates the link between redox state and protein homeostasis. Nat. Commun. 9, 256.

Copple, I.M., Lister, A., Obeng, A.D., Kitteringham, N.R., Jenkins, R.E., Layfield, R., Foster, B.J., Goldring, C.E., and Park, B.K. (2010). Physical and functional interaction of sequestosome 1 with Keap1 regulates the Keap1-Nrf2 cell defense pathway. J. Biol. Chem. 285, 16782–16788.

Cui, X.-G., Han, Z.-T., He, S.-H., Wu, X.-D., Chen, T.-R., Shao, C.-H., Chen, D.-L., Su, N., Chen, Y.-M., Wang, T., et al. (2017). HIF1/2α mediates hypoxia-induced LDHA expression in human pancreatic cancer cells. Oncotarget 8, 24840–24852.

Duran, A., Amanchy, R., Linares, J.F., Joshi, J., and Abu-Baker, S. (2011). p62 is a key regulator of nutrient sensing in the mTORC1 pathway. Mol. Cell 44, 134–146.

Durán, A., Serrano, M., Leitges, M., Flores, J.M., Picard, S., Brown, J.P., Moscat, J., and Diaz-Meco, M.T. (2004). The atypical PKC-interacting protein p62 is an important mediator of RANK-activated osteoclastogenesis. Dev. Cell 6, 303–309.

El-Hattab, A.W. (2015). Inborn errors of metabolism. Clin. Perinatol. 42, 413–439.

Falk, A., Koch, P., Kesavan, J., Takashima, Y., Ladewig, J., Alexander, M., Wiskow, O., Tailor, J., Trotter, M., Pollard, S., et al. (2012). Capture of neuroepithelial-like stem cells from pluripotent stem cells provides a versatile system for in vitro production of human neurons. PLoS One 7, e29597.

Fan, W., Tang, Z., Chen, D., Moughon, D., Ding, X., Chen, S., Zhu, M., and Zhong, Q. (2014). Keap1 facilitates p62-mediated ubiquitin aggregate clearance via autophagy. Autophagy 6, 614–621.

Gaikwad, A., Long, D.J., Stringer, J.L., and Jaiswal, A.K. (2001). In vivo role of NAD(P)H:quinone oxidoreductase 1 (NQO1) in the regulation of intracellular redox state and accumulation of abdominal adipose tissue. J. Biol. Chem. 276, 22559–22564.

Geisler, S., Holmström, K.M., Skujat, D., Fiesel, F.C., Rothfuss, O.C., Kahle, P.J., and Springer, W. (2010). PINK1/Parkin-mediated mitophagy is dependent on VDAC1 and p62/SQSTM1. Nat. Cell Biol. 12, 119–131.

Goyal, M.S., Hawrylycz, M., Miller, J.A., Snyder, A.Z., and Raichle, M.E. (2014). Aerobic glycolysis in the human brain is associated with development and neotenous gene expression. Cell Metab. 19, 49–57.

Grenier, K., McLelland, G.-L., and Fon, E.A. (2013). Parkin- and PINK1-dependent mitophagy in neurons: will the real pathway please stand up? Front. Neurol. 4, 100.

Haack, T.B., Ignatius, E., Calvo-Garrido, J., Iuso, A., Isohanni, P., Maffezzini, C., Lönnqvist, T., Suomalainen, A., Gorza, M., Kremer, L.S., et al. (2016). Absence of the autophagy adaptor SQSTM1/p62 causes childhood-onset neurodegeneration with ataxia, dystonia, and gaze palsy. Am. J. Hum. Genet. 99, 735–743.

Herrero-Mendez, A., Almeida, A., Fernández, E., Maestre, C., Moncada, S., and Bolaños, J.P. (2009). The bioenergetic and antioxidant status of neurons is controlled by continuous degradation of a key glycolytic enzyme by APC/C-Cdh1. Nat. Cell Biol. 11, 747–752.

Iavarone, A., and Lasorella, A. (2014). Myc and differentiation: going against the current. EMBO Rep. 15, 324–325.

Jain, A., Lamark, T., Sjottem, E., Bowitz Larsen, K., Atesoh Awuh, J., Øvervatn, A., McMahon, M., Hayes, J.D., and Johansen, T. (2010). p62/SQSTM1 is a target gene for transcription factor NRF2 and creates a positive feedback loop by inducing antioxidant response element-driven gene transcription. J. Biol. Chem. 285, 22576–22591.

Jain, I.H., Zazzeron, L., Goli, R., Alexa, K., Schatzman-Bone, S., Dhillon, H., Goldberger, O., Peng, J., Shalem, O., Sanjana, N.E., et al. (2016). Hypoxia as a therapy for mitochondrial disease. Science 352, 54–61.

Jiang, T., Harder, B., Rojo de la Vega, M., Wong, P.K., Chapman, E., and Zhang, D.D. (2015). p62 links autophagy and Nrf2 signaling. Free Radic. Biol. Med. 88, 199–204.

Joung, I., Kim, H.J., and Kwon, Y.K. (2005). p62 modulates Akt activity via association with PKCzeta in neuronal survival and differentiation. Biochem. Biophys. Res. Commun. 334, 654–660.

Khacho, M., Clark, A., Svoboda, D.S., MacLaurin, J.G., Lagace, D.C., Park, D.S., and Slack, R.S. (2017). Mitochondrial dysfunction underlies cognitive defects as a result of neural stem cell depletion and impaired neurogenesis. Hum. Mol. Genet. 26, 3327–3341.

Kim, D.-Y., Rhee, I., and Paik, J. (2014). Metabolic circuits in neural stem cells. Cell. Mol. Life Sci. 71, 4221–4241.

Koch, P., Opitz, T., Steinbeck, J.A., Ladewig, J., and Bruestle, O. (2009). A rosette-type, self-renewing human ES cell-derived neural stem cell with potential for in vitro instruction and synaptic integration. Proc. Natl. Acad. Sci. U S A 106, 3225–3230.

Komatsu, M., Kurokawa, H., Waguri, S., Taguchi, K., Kobayashi, A., Ichimura, Y., Sou, Y.-S., Ueno, I., Sakamoto, A., Tong, K.I., et al. (2010). The selective autophagy substrate p62 activates the stress responsive transcription factor Nrf2 through inactivation of Keap1. Nat. Cell Biol. 12, 213–223.

Kwon, J., Han, E., Bui, C.-B., Shin, W., Lee, J., Lee, S., Choi, Y.-B., Lee, A.-H., Lee, K.-H., Park, C., et al. (2012). Assurance of mitochondrial integrity and mammalian longevity by the p62-Keap1-Nrf2-Nqo1 cascade. EMBO Rep. 13, 150–156.

Lamark, T., Kirkin, V., Dikic, I., and Johansen, T. (2009). NBR1 and p62 as cargo receptors for selective autophagy of ubiquitinated targets. Cell Cycle 8, 1986–1990.

Lau, A., Wang, X.J., Zhao, F., Villeneuve, N.F., Wu, T., Jiang, T., Sun, Z., White, E., and Zhang, D.D. (2010). A noncanonical mechanism of Nrf2 activation by autophagy deficiency: direct interaction between Keap1 and p62. Mol. Cell. Biol. 30, 3275–3285.

Lee, Y., Sasai, M., Ma, J.S., Sakaguchi, N., Ohshima, J., Bando, H., Saitoh, T., Akira, S., and Yamamoto, M. (2015). p62 plays a specific role in interferon-γ-induced presentation of a toxoplasma vacuolar antigen. Cell Rep. 13, 223–233.

López-Hernández, B., Ceña, V., and Posadas, I. (2015). The endoplasmic reticulum stress and the HIF-1 signalling pathways are involved in the neuronal damage caused by chemical hypoxia. Br. J. Pharmacol. 172, 2838–2851.

López-Hernández, B., Posadas, I., Podlesniy, P., Abad, M.A., Trullas, R., and Ceña, V. (2012). HIF-1α is neuroprotective during the early phases of mild hypoxia in rat cortical neurons. Exp. Neurol. 233, 543–554.

Muto, V., Flex, E., Kupchinsky, Z., Primiano, G., Galehdari, H., Dehghani, M., Cecchetti, S., Carpentieri, G., Rizza, T., Mazaheri, N., et al. (2018). Biallelic SQSTM1 mutations in early-onset, variably progressive neurodegeneration. Neurology 91, e319–e330.

Narendra, D., Kane, L.A., Hauser, D.N., Fearnley, I.M., and Youle, R.J. (2010). p62/SQSTM1 is required for Parkin-induced mitochondrial clustering but not mitophagy; VDAC1 is dispensable for both. Autophagy 6, 1090–1106.

Narendra, D., Walker, J.E., and Youle, R. (2012). Mitochondrial quality control mediated by PINK1 and Parkin: links to parkinsonism. Cold Spring Harb. Perspect. Biol. 4, a011338.

Okatsu, K., Saisho, K., Shimanuki, M., Nakada, K., Shitara, H., Sou, Y.-S., Kimura, M., Sato, S., Hattori, N., Komatsu, M., et al. (2010). p62/SQSTM1 cooperates with Parkin for perinuclear clustering of depolarized mitochondria. Genes Cells 15, 887–900.

Paridaen, J.T.M.L., and Huttner, W.B. (2014). Neurogenesis during development of the vertebrate central nervous system. EMBO Rep. 15, 351–364.

Park, J.S., Kang, D.H., and Bae, S.H. (2015). p62 prevents carbonyl cyanide m-chlorophenyl hydrazine (CCCP)-induced apoptotic cell death by activating Nrf2. Biochem. Biophys. Res. Commun. 464, 1139–1144.

Park, S., Choi, S.-G., Yoo, S.-M., Son, J.H., and Jung, Y.-K. (2014). Choline dehydrogenase interacts with SQSTM1/p62 to recruit LC3 and stimulate mitophagy. Autophagy 10, 1906–1920.

Pursiheimo, J.P., Rantanen, K., Heikkinen, P.T., Johansen, T., and Jaakkola, P.M. (2009). Hypoxia-activated autophagy accelerates degradation of SQSTM1/p62. Oncogene *28*, 334–344.

Ramesh Babu, J., Lamar Seibenhener, M., Peng, J., Strom, A.-L., Kemppainen, R., Cox, N., Zhu, H., Wooten, M.C., Diaz-Meco, M.T., Moscat, J., and Wooten, M.W. (2008). Genetic inactivation of p62 leads to accumulation of hyperphosphorylated tau and neurodegeneration. J. Neurochem. *106*, 107–120.

Rantanen, K., Pursiheimo, J.-P., Högel, H., Miikkulainen, P., Sundström, J., and Jaakkola, P.M. (2013). p62/SQSTM1 regulates cellular oxygen sensing by attenuating PHD3 activity through aggregate sequestration and enhanced degradation. J. Cell Sci. *126*, 1144–1154.

Schlafli, A.M., Adams, O., Galvan, J.A., Gugger, M., Savic, S., Bubendorf, L., Schmid, R.A., Becker, K.-F., Tschan, M.P., Langer, R., and Berezowska, S. (2016). Prognostic value of the autophagy markers LC3 and p62/SQSTM1 in early-stage non-small cell lung cancer. Oncotarget *7*, 39544–39555.

Schönfeld, P., and Reiser, G. (2017). Brain energy metabolism spurns fatty acids as fuel due to their inherent mitotoxicity and potential capacity to unleash neurodegeneration. Neurochem. Int. *109*, 68–77.

Sholl, D.A. (1953). Dendritic organization in the neurons of the visual and motor cortices of the cat. J. Anat. *87*, 387–406.

Sonntag, K.-C., Ryu, W.-I., Amirault, K.M., Healy, R.A., Siegel, A.J., McPhie, D.L., Forester, B., and Cohen, B.M. (2017). Late-onset Alzheimer's disease is associated with inherent changes in bioenergetics profiles. Sci. Rep. *7*, 14038.

Tavernarakis, N., and Palikaras, K. (2012). Mitophagy in neurodegeneration and aging. Front. Cell Neurosci., 1–7. https://doi.org/10.3389/fgene.2012.00297/abstract.

Valencia, T., Kim, J.Y., Abu-Baker, S., and Moscat-Pardos, J. (2014). Metabolic reprogramming of stromal fibroblasts through p62-mTORC1 signaling promotes inflammation and tumorigenesis. Cancer Cell *26*, 121–135.

Valvona, C.J., Fillmore, H.L., Nunn, P.B., and Pilkington, G.J. (2016). The regulation and function of lactate dehydrogenase A: therapeutic potential in brain tumor. Brain Pathol. *26*, 3–17.

Vieira, H.L.A., Alves, P.M., and Vercelli, A. (2011). Modulation of neuronal stem cell differentiation by hypoxia and reactive oxygen species. Prog. Neurobiol. *93*, 444–455.

Wang, C., Chen, S., Yeo, S., Karsli-Uzunbas, G., White, E., Mizushima, N., Virgin, H.W., and Guan, J.-L. (2016). Elevated p62/SQSTM1 determines the fate of autophagy-deficient neural stem cells by increasing superoxide. J. Cell Biol. *212*, 545–560.

Wang, J., Duncan, D., Shi, Z., and Zhang, B. (2013). WEB-based GEne SeT analysis toolkit (WebGestalt): update 2013. Nucleic Acids Res. *41*, W77–W83.

Woo, Y.M., Shin, Y., Lee, E.J., Lee, S., Jeong, S.H., Kong, H.K., Park, E.Y., Kim, H.K., Han, J., Chang, M., and Park, J.-H. (2015). Inhibition of aerobic glycolysis represses Akt/mTOR/HIF-1α axis and restores tamoxifen sensitivity in antiestrogen-resistant breast cancer cells. PLoS One *10*, e0132285.

Zeng, R.-X., Zhang, Y.-B., Fan, Y., and Wu, G.-L. (2014). p62/SQSTM1 is involved in caspase-8 associated cell death induced by proteasome inhibitor MG132 in U87MG cells. Cell Biol. Int. *38*, 1221–1226.

Zheng, X., Boyer, L., Jin, M., Mertens, J., Kim, Y., Ma, L., Hamm, M., Gage, F.H., and Hunter, T. (2016). Metabolic reprogramming during neuronal differentiation from aerobic glycolysis to neuronal oxidative phosphorylation. Elife *5*, 859.

Supplemental Information

SQSTM1/p62-Directed Metabolic Reprogramming Is Essential for Normal Neurodifferentiation

Javier Calvo-Garrido, Camilla Maffezzini, Florian A. Schober, Paula Clemente, Elias Uhlin, Malin Kele, Henrik Stranneheim, Nicole Lesko, Helene Bruhn, Per Svenningsson, Anna Falk, Anna Wedell, Christoph Freyer, and Anna Wredenberg

Figure S1

Figure S2

A)

	Co1[NES]			Pat1[NES]		
Untreated						
Untreated +Bafilomycin						
CCCP						
CCCP +Bafilomycin						
O/A						
O/A +Bafilomycin						
	LC3II	Tom20	Merge	LC3II	Tom20	Merge

LC3II/TOM20

Pearson's correlation coefficient

Co1[NES]
Pat1[NES]

Untreated, Untreated+Baf, CCCP, CCCP+Baf, O/A, O/A+Baf

B)

LAMP2/TOM20

Pearson's correlation coefficient

Co1[NES]
Pat1[NES]

CCCP, O/A

Figure S3

A)

Co1^{NEU} / Pat1^{NEU} — Tom20 / LC3II / Merge — CCCP

Co1^{NEU} / Pat1^{NEU} — Tom20 / LC3II / Merge — O/A

LC3II/TOM20

Pearson's correlation coefficient

Co1^{NES} / Pat1^{NES}

CCCP   O/A

B)

Co1^{NEU} / Pat1^{NEU} — Tom20 / LAMP2 / Merge — CCCP

Co1^{NEU} / Pat1^{NEU} — Tom20 / LAMP2 / Merge — O/A

LAMP2/TOM20

Pearson's correlation coefficient

Co1^{NES} / Pat1^{NES}

CCCP   O/A

C) GSH (nmol/µg protein) — CCo1^{NES} / KO1^{NES} — Day 0   Day 4

D) mRNA levels (Relative units) — CCo1^{NES} / KO1^{NES} / CCo1^{NES} + CCCP / KO1^{NES} + CCCP — GSS NRF2 NQO1 GSTM4 TRX1 SOD1 GSR GCLC GCLM — xCT

E) p62 — Untreated CCCP O/A

F) Co1^{NES} / Pat1^{NES} Co1^{NES} / Pat1^{NES} — GPX4 / GSTP1 / Nqo1 / p62 / Tubulin

G) Nqo1 levels (relative units) — Co1^{NES} / Pat1^{NES}
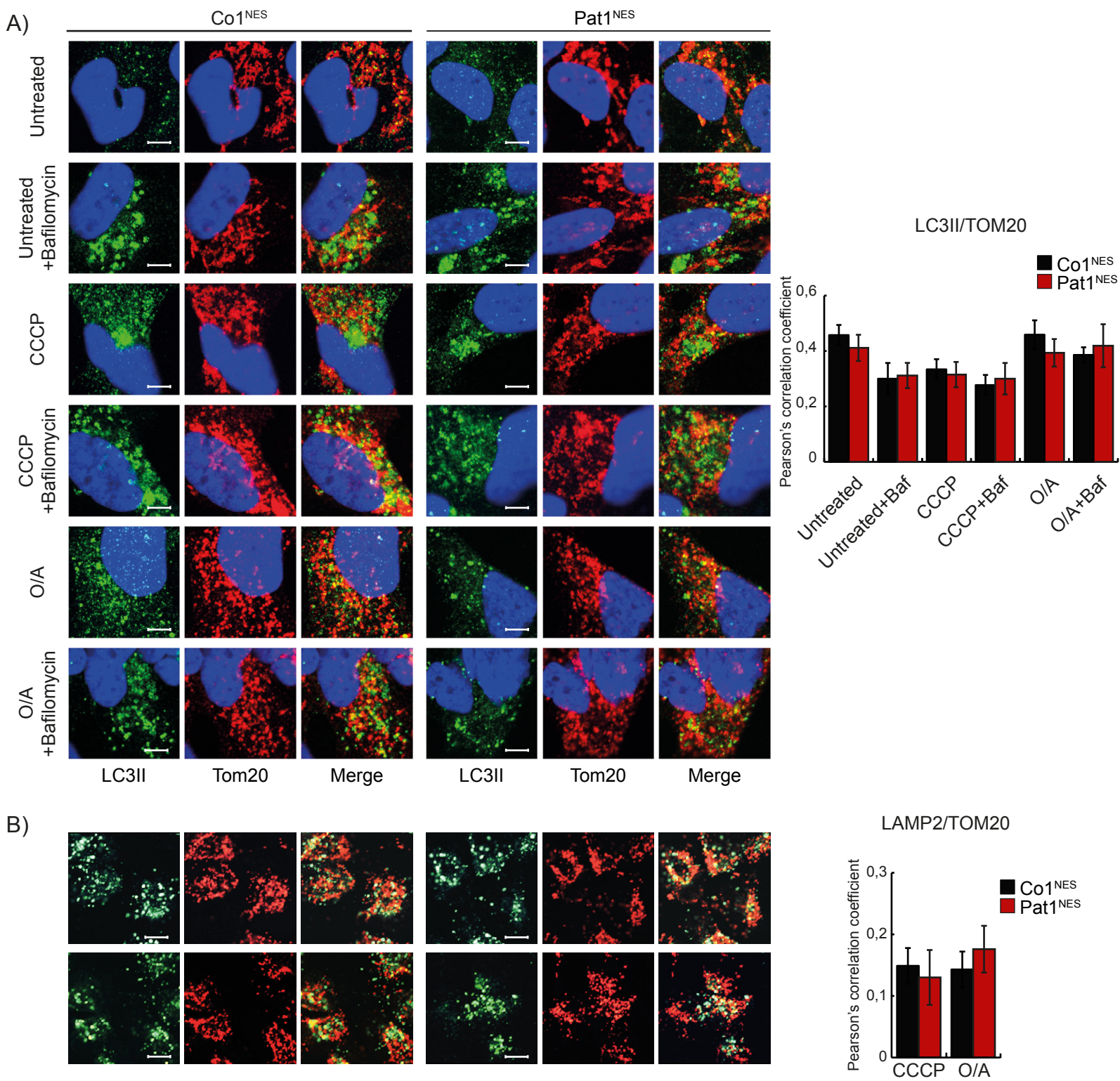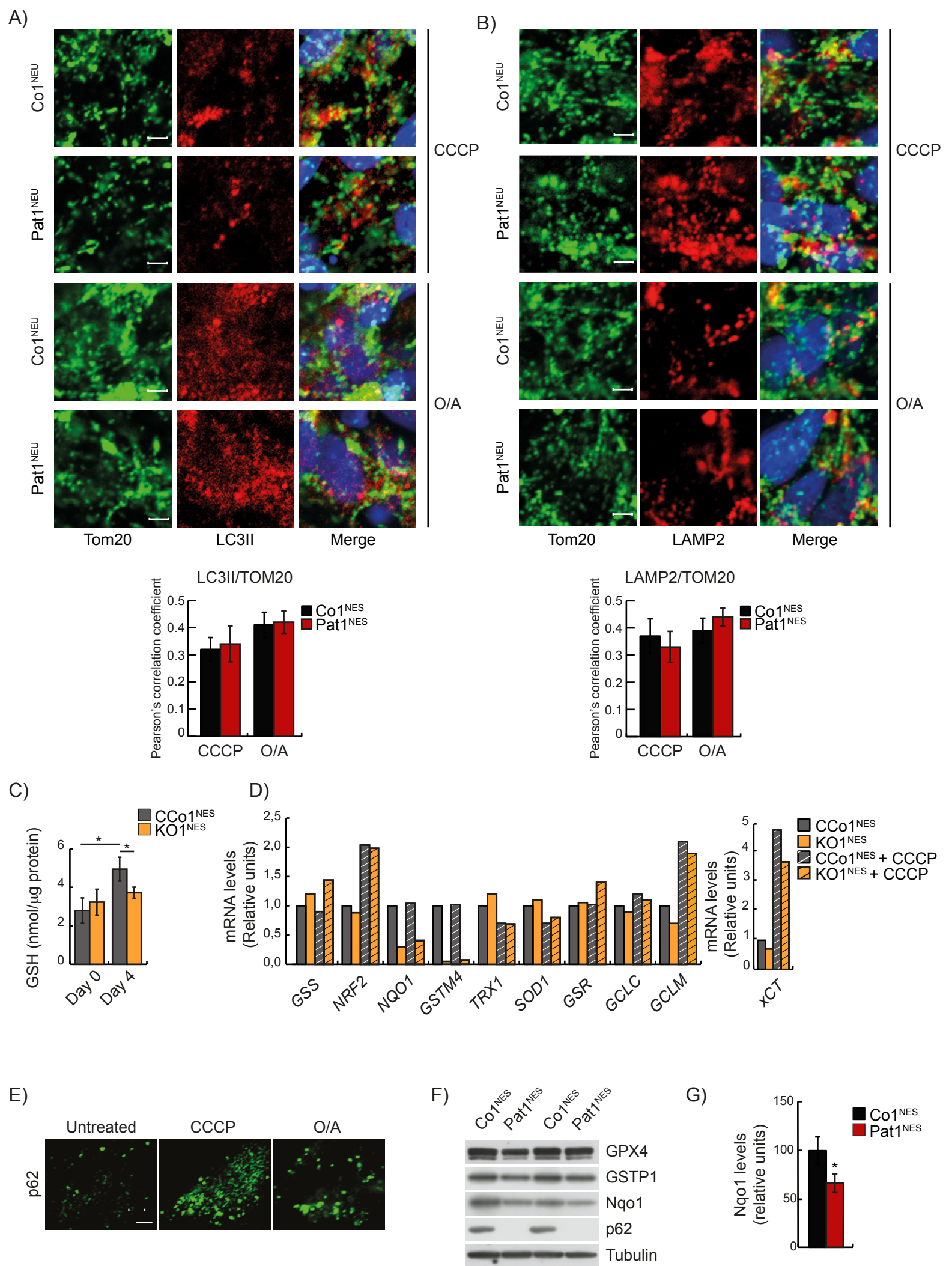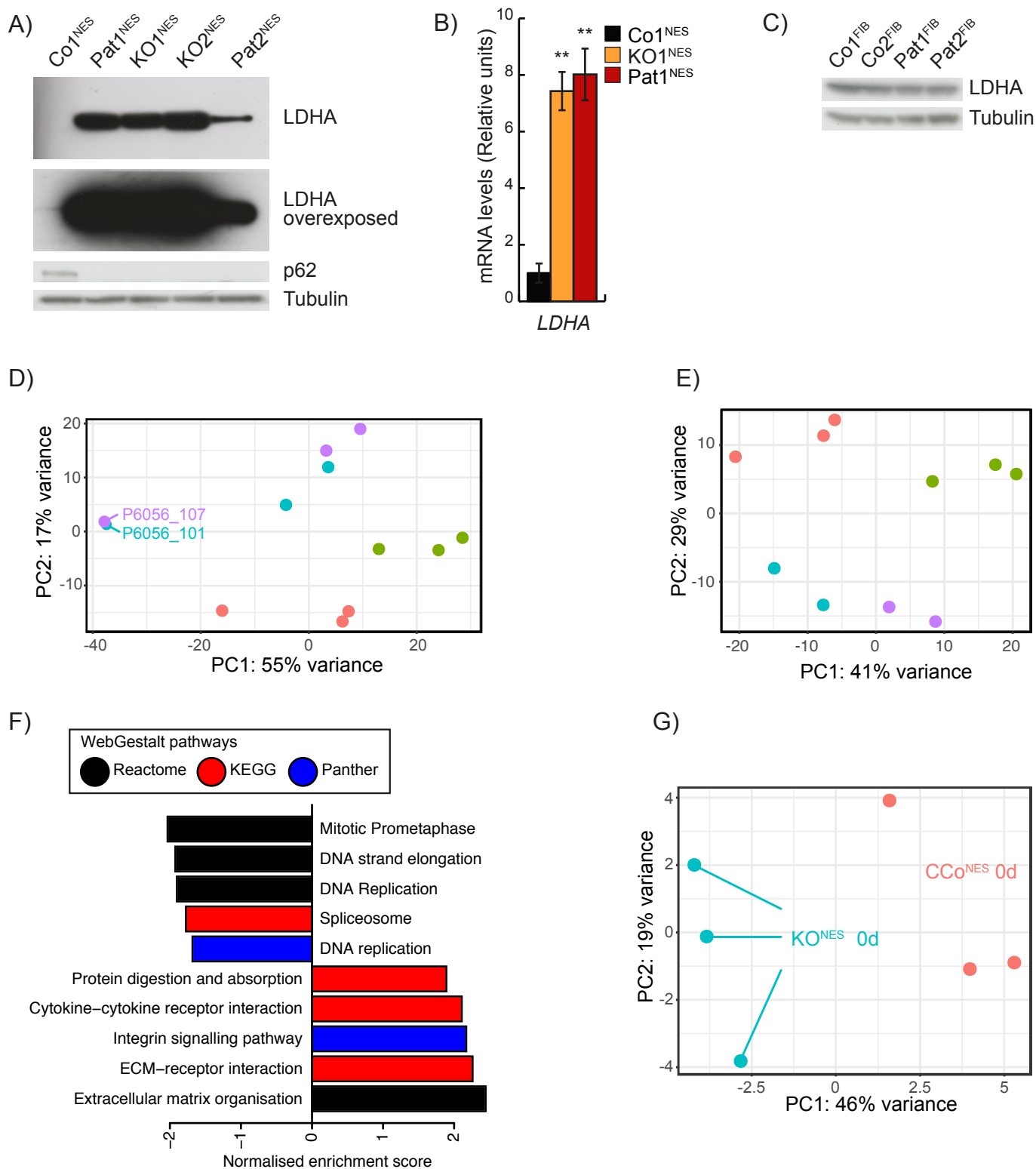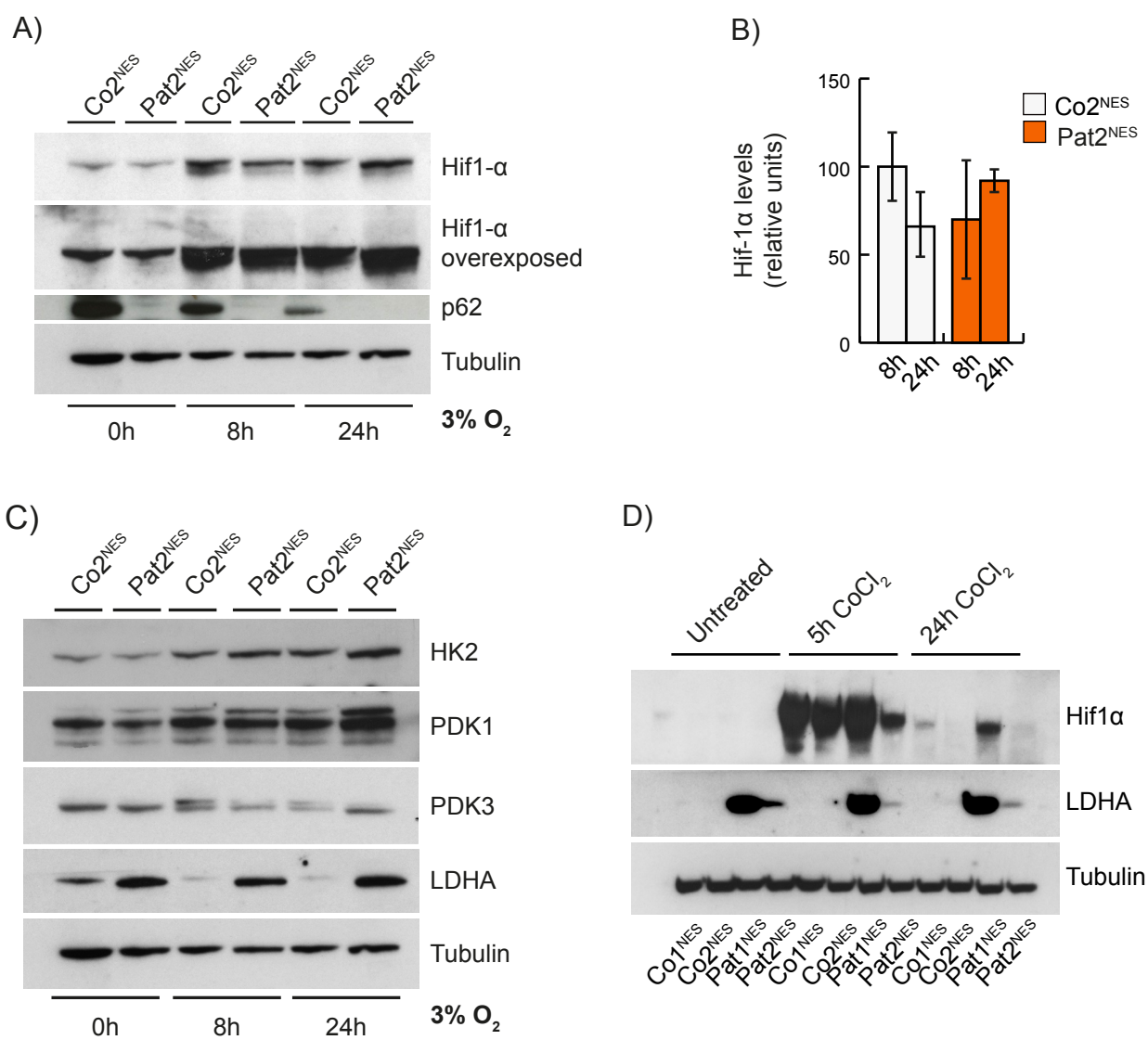
Figure S4

Figure S5

Figure S6

SUPPLEMENTARY FIGURES LEGENDS

Figure S1. Characterisation of NES cells. Related to figure 1.
(**A**) Representative fluorescence images of Co1^{NES}, Pat1^{NES} immunostained against stem cell markers Nestin, SOX2, PLZF and DACH1. Scale bar: 20 μm. (**B**) Representative western blot analysis of Nestin, SOX2, PLZF and DACH1 in Co1^{NES} and Pat1^{NES} cells. Tubulin was used as a loading control. For (A-B) n=3 independent experiments. (**C**) qRT-PCR analysis of p62 transcript levels in Co1^{NES} (grey), Pat1^{NES} (red), Pat2^{NES} (orange), KO1^{NES} (dark yellow) and KO2^{NES} (light yellow) cells. Data are expressed as mean ± standard deviation (SD) and differences were tested by a two-tailed t-test. ** $p < 0.01$ and *** $p < 0.001$, n=3 independent experiments.
Figure S2. Characterisation of neuronal differentiation. Related to figure 1. (**D**) Representative fluorescence images of Co1^{NEU}, Co2^{NEU}, Co3^{NEU}, Pat1^{NEU} and Pat2^{NEU}, immunostained against stem cell marker SOX2 and neuronal marker MAP2A/B at 20 days of differentiation. Scale bar: 100 μm. (**E**) Representative fluorescence images of Co1^{NEU}, Co2^{NEU}, Co3^{NEU}, Pat1^{NEU} and Pat2^{NEU} immunostained against neuronal cell markers HuC/D (red), β-III tubulin (green) at 20 days of differentiation. Scale bar: 100 μm. (**F**) Representative fluorescence images of Co1^{NEU}, Co2^{NEU}, Co3^{NEU}, Pat1^{NEU} and Pat2^{NEU} immunostained against neuronal cell markers MAP2A/B (red), Neurofilament (green) at 20 days of differentiation. Scale bar: 100 μm. (**G**) Linear Sholl analysis representation of 20-days differentiated Co1^{NEU}, Co2^{NEU}, Co3^{NEU}. n=3 independent experiments. Neuronal processes analysed from 25 neuronal bodies.

Figure S2. Characterisation of neuronal differentiation and confocal analysis of mitophagy in fibroblasts. Related to figures 1 and 2.
(**A**) Representative bright field images of CCo1^{NEU} and KO1^{NEU} cells after 14 days of differentiation. (**B**) Linear Sholl analysis representation of 20-days differentiated CCo1^{NEU} and KO1^{NEU}. n=3 independent experiments. Neuronal processes analysed from 25 neuronal bodies per line. (**C**) Top: representative bright field images of NES cells transduced with non-targeting shRNAs or p62 shRNA #2 and subjected to 7 days of differentiation process. Bottom: western blot analysis of p62 in Co1^{NES} transduced with non-targeting shRNAs and three different p62 shRNAs. (**D**) Top: representative bright field images of Pat1^{NES} cells transduced with empty pBABE or a pBABE-p62 construct and subjected to 14 days of differentiation. Bottom: western blot analysis of p62 in Co1^{NES} and Pat1^{NES} cells transduced with empty pBABE or pBABE-p62. For C and D tubulin was used as a loading control. Scale bar: 100 μm. n=3 independent experiments. (**E**) Left: representative fluorescence images of Co1^{NEU} and Pat1^{NEU}, immunostained against stem cell marker SOX2 (red) and neuronal marker MAP2A/B (green) at 20 and 45 days of differentiation. Scale bar: 100 μm. Right: quantification of the relative number of SOX2 positive cells in Co1^{NEU}, Co2^{NEU}, Co3^{NEU} (pooled as "Co^{NEU}"), Pat1^{NEU} and Pat2^{NEU} cells after 20 and 45 days of differentiation. Data are expressed as mean ± standard deviation (SD) and differences were tested by a two-tailed t-test. ** $p < 0.01$, *** $p < 0.001$. n=3 independent experiments. (**F**) Representative confocal images of Co^{FIB} treated for 2h with CCCP (20 μM) (top) or O/A (10 μM / 1 μM) (bottom). Fibroblasts are immunostained against Tom20 (red) and p62 (green). (**G**) Graphs represent the quantification of Pearson's correlation coefficient between p62 and Tom 20 in fibroblasts overexpressing Parkin, fibroblasts, NES cells and 14-days differentiated neurones. Cells were treated for 2h with CCCP (20 μM for fibroblasts and 10 μM for NES and neurones) or O/A (10 μM / 1 μM for fibroblasts and 5 μM / 1μM for NES and neurones) and with 50 nM bafilomycin. Data are presented as mean ± standard deviation (SD) and differences were tested by a two-tailed t-test. *** $p < 0.001$, n=3 independent experiments. 25 cells per experiment were analysed to calculate Pearson's correlation coefficient. (**H**) Representative western blot analysis of Parkin in fibroblasts, NES cells, 14-day differentiated neurones and HeLa cells. n=2 independent experiments. (**I-K**) Representative western blot analysis in Co^{FIB}, Pat1^{FIB} and Pat2^{FIB} treated for 24h with CCCP (20 μM) or O/A (10 μM / 1 μM) and for 2h with 50nM bafilomycin. Tubulin was used as a loading control. n=3 independent experiments. (**L, M**) Representative confocal images of Co^{FIB} and Pat1^{FIB} treated for 24h with CCCP (20 μM) or O/A (10 μM / 1 μM) immunostained against LC3II (green) and Tom20 (red) in (L) or against LAMP2 (green) and Tom20 (red) in (M). Graphs represent the quantification of Pearson's correlation coefficient between the analyzed proteins. Data are presented as mean ± standard deviation (SD) and differences were tested by a two-tailed t-test. n=3 independent experiments. 25 cells per experiment were analysed to calculate Pearson's correlation coefficient. Scale bars: F 20 μm, L and M 5 μm.

Figure S3. Confocal analysis of mitophagy in NES cells. Related to figure 2.
(**A**) and (**B**) Left: representative confocal images of Co1^{NES} and Pat1^{NES} treated with CCCP (10 μM) and O/A (10 μM / 1 μM) for 12 hours, with or without 50 nM bafilomycin. NES cells were immunostained against LC3II (green), Tom20 (red) and DAPI (blue) in (A) or LAMP2 (green), Tom20 (red) and DAPI (blue). Right: graphs representing the quantification of Pearson's correlation coefficient between the analyzed proteins. Data are presented as mean ± standard deviation (SD). n=3 independent experiments. 25 cells per experiment were analysed to calculate Pearson's correlation coefficient. Scale bars: 20 μm.

Figure S4. Confocal analysis of mitophagy in neurons and differential antioxidant behaviour in NES cells lacking p62. Related to figures 2 and 3.
(**A**) and (**B**) Representative confocal images of Co1^{NEU} and Pat1^{NEU} differentiated for 14 days and treated with CCCP (10 μM) and O/A (10 μM / 1 μM) for 12 hours. Neurones were immunostained against LC3II (red), Tom20 (green) and DAPI (blue) in (A) or LAMP2 (red), Tom20 (green) and DAPI (blue). Right: graphs representing the quantification of Pearson's correlation coefficient between the analyzed proteins. Data are presented as mean ± standard deviation (SD). n=3 independent experiments. 25 cells per experiment were analysed to calculate Pearson's correlation coefficient. Scale bars: 20 μm. (**C**) Quantification of reduced glutathione levels in undifferentiated and 4 days differentiated CCo1^{NES} (grey) and KO1^{NES} (orange). Data are presented as mean ± standard deviation (SD) and differences were tested by a two-tailed t-test. * p < 0.05, n=3 independent experiments. (**D**) qRT-PCR analysis in untreated or treated with 10 μM CCCP for 6 hours CCo1^{NES} (grey) and KO1^{NES} (orange). Beta-actin was used as endogenous control. n=2 independent experiments. (**E**) Representative confocal images of NES cells treated for 6 hours with 10 μM CCCP or 5 μM oligomycin and 1 μM antimycin, followed by immunostaining against p62. n=3 independent experiments. Scale bar 10 μm. (**F**) Representative western blot analysis of GPX4, GSTP1, NQO1 and p62 in Co1^{NES} and Pat1^{NES} cells. Tubulin was used as a loading control. n=3 independent experiments. (**G**) Quantification of NQO1 levels from (F). Data are presented as mean ± standard deviation (SD) and differences were tested by a two-tailed t-test. * p < 0.05, n=3 independent experiments.

Figure S5. Western blot and qPCR analysis of LDHA in NES cells and fibroblasts and quality control of high-throughput data. Related to figure 4 and 5.
(**A**) Representative western blot analysis of LDHA and p62 in Co1^{NES}, Pat1^{NES}, KO1^{NES}, KO2^{NES} cells and Pat2^{NES}. Tubulin was used as a loading control. n=3 independent experiments. (**B**) qRT-PCR analysis of LDHA transcript levels in Co1^{NES} (grey), KO1^{NES} (dark yellow) and Pat1^{NES} (red) cells. Beta-actin was used as endogenous control. Data are expressed as mean ± standard deviation (SD) and differences were analysed by a two-tailed t-test. ** p < 0.01, n=3 independent experiments. (**C**) Representative western blot analysis of LDHA in two fibroblast control lines, Pat1^{FIB} and Pat2^{FIB}. Tubulin was used as a loading control. n=3 independent experiments. (**D**) Principal component analysis of undifferentiated (0d) and differentiated (4d) control CCo^{NES} and KO^{NES} transcriptomes. Two outlier samples are labeled P6056_101 and P6056_107. (**E**) Principal component analysis of undifferentiated (0d) and differentiated (4d) control CCo^{NES} and KO^{NES} transcriptomes, excluding the outlier samples identified in (A). (**F**) Gene Set Enrichment Analysis (GSEA) against pathways in WebGestalt of the outlier transcriptome samples identified in (A) compared to all other samples. (**G**) Principal component analysis of undifferentiated (0d) CCo^{NES} and KO^{NES} proteomes.

Figure S6: Physiological oxygen concentration reveals a pro-glycolytic metabolism in the absence of p62. Related to figure 6.
(**A**) Representative western blot analysis of Hif-1α and p62 steady-state levels in Co2^{NES} and Pat2^{NES} cells, cultured for 0, 8 or 24h at 3% O2. Tubulin was used as a loading control. n=3 independent experiments. (**B**) Quantification of (A). Data are expressed as mean ± standard deviation (SD). n=3 independent experiments. (**C**) Representative western Blot analysis of HK2, PDK1, PDK3 and LDHA as in (A). Tubulin was used as a loading control. n=3 independent experiments. (**D**) Representative western blot analysis of Hif-1α and LDHA in Co1^{NES}, Co2^{NES}, Pat1^{NES} and Pat2^{NES} cultured for 0, 5 or 24h in the presence of 200 μM CoCl2. Tubulin was used as loading control. n=5 independent experiments.

Table S2. qPCR primer sequences.

Species	Gene (Forward/Reverse)	Sequence (5´-3´)
Human	GCLC forward	TGTCTCCAGGTGACATTCCA
Human	GCLC reverse	GCCTCGGTAAAAGGGAGATG
Human	GCLM forward	CACAGCGAGGAGGAGTTTC
Human	GCLM reverse	TGATTCTACAATGAACAGTTTTGCA
Human	GPX1 forward	TTCCCGTGCAACCAGTTT
Human	GPX1 reverse	AGGGAATTCAGAATCTCTTCGTT
Human	GPX4 forward	TACGGACCCATGGAGGAG
Human	GPX4 reverse	CCACACACTTGTGGAGCTAGAA
Human	GSR forward	TTTACCCCGATGTATCACGC
Human	GSR reverse	TTCATCACACCCAAGTCCCT
Human	GSS forward	TCGTCTCTTTGACATCCACA
Human	GSS reverse	TTCGATCTGTTTCAGGGCTG
Human	GST forward	GCTACAGCCCTGACTTTGAG
Human	GST reverse	AGGTGATCTTGTCTCCAACA
Human	GSTA1 forward	GGTGACAGCGTTTAACAAAGC
Human	GSTA1 reverse	CCGTGCATTGAAGTAGTGGA
Human	GSTK1 forward	TTTGGCTCTGACCGGATG
Human	GSTK1 reverse	CACGGCTGGAGGTATAGGG
Human	GSTP1 forward	TCCCTCATCTACACCAACTATGAG
Human	GSTP1 reverse	GGTCTTGCCTCCCTGGTT
Human	LDHA forward	AACATGGCAGCCTTTTCCTT
Human	LDHA reverse	TAAGACGGCTTTCTCCCTCT
Human	Nqo1 forward	CACTGGTGGCAGTGGCTC
Human	Nqo1 reverse	CCAATGCTATATGTCAGTTGAGG
Human	Nrf2 forward	GACGGTATGCAACAGGACA
Human	Nrf2 reverse	TTGAGGGTATAGATGAGTAAAAATGAT
Human	p62 forward	TACGACTTGTGTAGCGTCTG
Human	p62 reverse	CGTGTTTCACCTTCCGGAG
Human	SOD1 forward	TGACAAAGATGGTGTGGCC
Human	SOD1 reverse	TTCATTTCCACCTTTGCCCA
Human	Trx1 forward	GTGGGCCTTGCAAAATGATC
Human	Trx1 reverse	GGCATGCATTTGACTTCACA
Human	xCT forward	TTTGGAGCTTTGTCTTATGCTG
Human	xCT reverse	GAGTTCCACCCAGACTCGTA

STAR METHODS

CONTACT FOR DETAILS AND RESOURCE SHARING

Further information and requests for resources and reagents should be directed at: Anna Wredenberg (anna.wredenberg@ki.se).

EXPERIMENTAL MODELS AND SUBJECTS DETAILS

Fibroblasts, HeLa and Phoenix-AMPHO cells

Human primary skin fibroblasts (passage 4 to 12) were taken from patients II:1 (Pat1, female) at 30 years of age and II:4 (Pat2, male) 17 years of age at the time of biopsy. The patients were born healthy to consanguineous parents of Kurdish descent and have been previously described in family 4 of (Haack et al., 2016), HeLa cells and Phoenix-AMPHO (ATCC) cells (passage 4 to 10) were cultured at 37°C in a 5% CO_2 atmosphere in DMEM-Glutamax (Thermo Fisher Scientific) media containing 25 mM glucose, 10% FBS (Thermo Fisher Scientific) and 1 mM sodium pyruvate (Thermo Fisher Scientific). Experiments were performed with cells cultured to 80%–90% confluency. Medium was changed regularly and cells were passaged using trypsin (Thermo Fisher Scientific).

Reprogramming of fibroblasts

Fibroblasts were reprogrammed using integration free Sendai virus-vector-mediated reprogramming (CytoTune™-iPS 2.0 reprogramming kit, Thermo Fisher Scientific). Fibroblasts were seeded at a density of 2.5 X 10^4 cells/cm². The following day the cells were transduced using the Sendai virus according to the manufacturer's protocol. Seven days after transduction the cells were passaged using Trypsin-EDTA (0.05%) (Thermo Fisher Scientific) to a laminin-521 (Biolamina) coated plate at a density of 1.9 x 10^3 cells/cm² in Essential 8TM medium (Thermo Fisher Scientific) containing 5 µM of Y27632 rho-kinase inhibitor (ROCKi) (Millipore). Emerging iPS cell colonies were manually picked for the first passage and then enzymatically passaged as single cells as described below.

Human induced pluripotent stem (hiPS) cells

hiPS cells were cultured on human recombinant Laminin-521 (Biolamina) in Essential 8™ medium (Thermo Fisher Scientific). The cells were enzymatically passaged as single cells, using TrypLE Select 1x (Thermo Fisher Scientific) and seeded in Essential 8™ medium (Thermo Fisher Scientific) containing 10 µM of Y27632 rho-kinase inhibitor (ROCKi) (Millipore).

Neural induction of induced pluripotent stem cells

The neural induction protocol is based on (Chambers et al., 2009). Approximately 3.8 x 10^4 hiPS cells/cm² were seeded in a well of a Laminin-521 coated tissue culture plate with 10 µM of ROCKi in Essential 8™ medium. The day after seeding medium was changed to 80% DMEM/F12+GlutaMax (Thermo Fisher Scientific) plus 20% Knockout serum replacement (KSOR) medium (Thermo Fisher Scientific), Non-essential Amino Acids (Thermo Fisher Scientific), 2-mercaptoethanol (Thermo Fisher Scientific), Penicillin-streptomycin (Thermo Fisher Scientific) with 10 nM of SB-431542 (StemCell Technologies), 500 ng/mL of Noggin (PeproTech) and 10 nM CHIR 99021 (StemCell Technologies). Medium was changed daily. SB421542 was omitted from the medium after 5 days of differentiation and KSOR medium was progressively replaced by adding increasing levels of N2B27 medium, containing, 50% DMEM/F12 GlutaMax, 50% Neurobasal (Thermo Fisher Scientific), 2-mercapthoethanol, N-2 Supplement (100X) 5 µl/ml (Thermo Fisher Scientific), B-27 Supplement (50X) 10 µl/ml

(Thermo Fisher Scientific) and Penicillin-streptomycin (25%, 50%, 75% and 100%). At the 12th day of differentiation the cells were passaged and introduced to NES culture conditioned conditions.

Neuroepithelial-like stem (NES) cells

The generation of NES cells has previously been described (Falk et al., 2012; Koch et al., 2009). NES cells (passage 15 to 50) were cultured on 100 μg/ml poly-ornithine/ 2 μg/ml laminin2020-coated culture dishes (both (Sigma-Aldrich)), in DMEM/F-12 GlutaMax (Thermo Fisher Scientific) media containing 17 mM glucose, 100 units/ml penicillin-streptomycin (Thermo Fisher Scientific), N-2 Supplement (1:100) (Thermo Fisher Scientific), B-27 Supplement (1:1000) (Thermo Fisher Scientific), 10 ng/μl bFGF (Thermo Fisher Scientific) and 10 ng/μl EGF (Peprotech) at 37°C in a 5% CO_2 atmosphere. Three-fourths of the media was exchanged daily. Cells were trypsinised using TrypLE Express 1x (Thermo Fisher Scientific). Neuronal differentiation was induced by removing the growth factors bFGF and EGF from the medium and increasing the B-27 Supplement concentration to 1:100. The culture media was exchanged as described above. Control NES cell lines were derived from one male (Co1, C3 in (Wu et al., 2014)) and one female (Co2, AF22 in (Falk et al., 2012)) donors and have been previously described (Falk et al., 2012; Wu et al., 2014). A third control line was introduced (Co3), isolated from another female donor.

Hypoxia experiments were performed in a 3% oxygen concentration incubator for the indicated time periods.

Generation of p62 knockout NES cells by CRISPR/Cas9 gene editing

The p62 locus of control NES cells (Co1) was targeted by CRISPR/Cas9 gene editing technology, as previously described (Cong et al., 2013). In short, pX335-U6-Chimeric_BB-CBh-hSpCas9n (D10A) plasmids (pX335-U6-Chimeric_BB-CBh-hSpCas9n(D10A) was a gift from Feng Zhang (Addgene plasmid # 42335)), with or without the p62 guide RNA sequence (targeting sequences are described in the key resource table), were nucleofected into control NES cells, using a 4D-Nucleofector™ System (Lonza). After nucleofection, cells were seeded in p35 dishes in conditioned NES cell media, at a 10 cell / well density. Following expansion, single clones were picked, using cloning cylinders (Sigma-Aldrich) and screened by Western blot analysis for the absence of p62 using SQSTM1/p62 antibodies (Cell Signaling Technology). Two CRISPR control (CCo1[NES] and CCo2[NES]) or p62-deficient (KO1[NES] and KO2[NES]) cell clones were used for further analysis.

METHOD DETAILS

Retroviral production and NES cells transduction

For overexpression experiments, p62 cDNA was cloned into pBABE-Puro. For silencing experiments, a p62 shRNA (Origene) or a non-targeting 29-mer scrambled shRNA cassette (Origene) were cloned in pGFP-V-RS. Overexpression and silencing of p62 in control NES and Pat1[NES] cells were performed by retroviral transduction of the corresponding plasmids.

For production of retrovirus, Phoenix-AMPHO cells (ATCC) were treated for 1h with 25 μM chloroquine (Sigma-Aldrich) and transfected using calcium chloride (Sigma-Aldrich) following manufacturer's instructions. After 7 hours fresh medium was added. Medium was harvested and filtered 24 hours and 48 hours after transfection. Retrovirus-containing medium was concentrated, using a Retro-X™ Concentrator (Clontech) following manufacturer's instructions and resuspended in 0.15% BSA. NES cells were transduced after addition of 5 μg/ml polybrene (Sigma-Aldrich).

Western Blotting

Cells were harvested by trypsinisation and pellets were lysed using RIPA buffer (150 mM NaCl, 1% Triton x-100, 1% Sodium deoxycholate, 0.1% SDS, 1 mM EDTA and 50 mM Tris-HCl pH 7.4) followed by sonication. Whole-cell protein extracts were separated using Novex NuPAGE SDS-PAGE gel system (Thermo Fisher Scientific) and transferred to polyvinylidene difluoride membranes (Millipore), using 25 mM Tris, 192 mM glycine, pH 8.3 and 20% methanol. Membranes were blocked with 5% skim milk in TBS-T (25 mM Tris, 140 mM NaCl, 1% Tween 20, pH 7.4). Primary antibodies were incubated for at least 15h at 4°C. Primary antibodies used were: SQSTM1/p62 (Cell Signaling Technology, 5114S), Tom20 (Santa Cruz Biotechnology, SC-17764), LC3II (Cell Signaling Technology, 3868S, Sigma-Aldrich, L8918), PARKIN (Abcam, ab15954), KEAP1 (Cell Signaling, 4678S), GAPDH (Santa Cruz Biotechnology, SC-20357), Hif-1α (Cell Signaling Technology, 14179S), α-Tubulin (Sigma-Aldrich, T6199), PINK1 (Cell Signaling Technology, 6946), LDHA (Cell Signaling Technology, 2012), HK2 (Cell Signaling Technology, 2106), Phospho-p70 S6 Kinase (Thr389) (Cell Signaling Technology, 9234), p70 S6 Kinase Antibody (Cell Signaling Technology, 9202), c-Myc (Cell Signaling Technology, 5605), total OXPHOS Human Antibody Cocktail (Abcam, ab110411), MAP2A/B (Millipore, MAB3418), HuC/D (Thermo Fisher Scientific, A-21271), PDK1 (Cell Signaling Technology, 30625), PDK3 (Sigma-Aldrich, HPA046583), Nestin (R&D Systems, MAB1259), PLZF (Thermo Fisher Scientific, MA5-15667), DACH1 (ProteinTech, 10914-1-AP), NQO1 (Cell Signaling Technology, 622625), GPX4 (R&D Systems, MAB5457), GSTP1 (Cell Signaling Technology, 3369) and NRF2 (Abcam, ab31163). Membranes were washed and incubated for 2h at RT with the appropriate secondary antibody at a 1:4000 dilution. Secondary antibodies used in this study were: horseradish peroxidase-conjugated anti-rabbit (GE Healthcare, NA9340), anti-mouse (GE Healthcare, NA9310) or anti-goat (Santa Cruz Biotechnology, SC-2020). Western blots were visualised using Clarity Western ECL solution (Bio-Rad), following manufacturer's instructions.

RNA isolation, RT-PCR and quantitative PCR

Total RNA was extracted using TRIzol (Thermo Fisher Scientific), followed by DNase-treatment using TURBO DNA-*free* kit (Thermo Fisher Scientific). 250 ng of RNA were reverse-transcribed using a High-capacity cDNA Reverse Transcription Kit (Applied Biosystems). Quantitative PCR analysis was performed using a Quant Studio 6 Flex instrument and Platinum SYBR Green qPCR supermix-UDG (Thermo Fisher Scientific). Gene expression was normalised to the house-keeping gene actin. Primers are listed in Table S2.

Detection of reactive oxygen species and measurement of glutathione levels

NES cells or NES cells subjected to differentiation for 4 days were incubated at 37°C for 30 minutes with 1 μM CM-H_2DCFDA (Thermo Fisher Scientific). Images were taken using a Carl Zeiss fluorescence microscope. ImageJ software was used for signal intensity analysis.

Glutathione levels were measured in undifferentiated and 4-days differentiated NES cells, using the Glutathione assay kit (Sigma-Aldrich) following manufacturer's instructions.

Immunocytochemistry, confocal microscopy and bright field microscopy

For PARKIN overexpression experiments, fibroblasts were nucleofected using a YFP-PARKIN plasmid (YFP-PARKIN was a gift from Richard Youle (Addgene plasmid # 23955)). 46h later, the fibroblasts were treated with 20 μM CCCP (Sigma-Aldrich) or 10 μM oligomycin and 1 μM antimycin and fixed 2h later using the following protocol.

Fibroblasts, NES cells or neurones were cultured on 1,5 mm cover-slips as described above and fixed for 20 min using 3% paraformaldehyde (VWR) at RT. Permeabilisation and blocking was performed using a combination of saponin 0,1% (Sigma-Aldrich), 1% BSA (Sigma-Aldrich) in PBS for 1 hour. Primary antibodies TOM20 (Santa Cruz Biotechnology, SC-17764), SQSTM1 (Santa Cruz Biotechnology, SC-28359), LAMP2 (Southern Biotech, 9840-01), LC3II (MBL International, M152-3), Beta-3 Tubulin (Sigma-Aldrich, T8578) MAP2A/B (Millipore, MAB3418), Neurofilament (Sigma-Aldrich, N4142), HuC/D (Thermo Fisher Scientific, A-21271), Nestin (R&D Systems, MAB1259), SOX2 (Cell Signaling Technology, 3579S), PLZF (Thermo Fisher Scientific, MA5-15667) and DACH1 (ProteinTech, 10914-1-AP) were diluted in PBS with 1% BSA and incubated overnight. After washing, cells were incubated for 1h with secondary antibodies Alexa Fluor® 488 (Thermo Fisher Scientific, A-11017 (mouse) or A-11034 (rabbit)), Alexa Fluor® 568 (Thermo Fisher Scientific, A-11031 (mouse) or A-11036 (rabbit)) or Alexa Fluor® 633 (Thermo Fisher Scientific, A-21052 (mouse) or A-21071 (rabbit)) at a 1:1000 dilution. Cells were mounted with ProLong® Diamond Antifade Mountant (Thermo Fisher Scientific) and 0.01 µg/ml DAPI (Sigma-Aldrich, D9542), where appropriate. A Nikon Ti-E inverted point scanning confocal microscope A1R Si was used for image acquisition. A Carl Zeiss bright field microscopy was used for neuronal image acquisition during differentiation experiments. ImageJ software was used for image quantification.

Cell viability test

MTT (3-(4,5-dimethylthiazol-2-yl)-2,5-diphenyltetrazolium bromide, Sigma-Aldrich) assays were used to monitor cell growth in the presence or absence of CCCP and NAC. Briefly, NES cells were treated for 15h with 10 µM CCCP and/or 1 mM NAC, followed by 90 min incubation in 300 µg/ml of MTT in phenol-free DMEM-Glutamax (Thermo Fisher Scientific) at 37°C. Cells were incubated for 10 min in 400 µl of DMSO (Sigma-Aldrich). 100 µl aliquots were used to measure emission at 570 nm and 630 nm, using a Infinite200 PRO multimode reader (TECAN).

Mitophagy assays

Fibroblasts were treated for 24 hours with 20 µM CCCP (Sigma-Aldrich), 10 µM oligomycin and 1 µM antimycin or 50 nM bafilomycin (Sigma-Aldrich). NES cells or neurones differentiated for 14 days were treated for 12 hours with 10 µM CCCP (Sigma-Aldrich) or 10 µM oligomycin and 1 µM antimycin. Cells were immunostained followed by confocal visualisation or harvested for Western blot and qRT-PCR analysis.

Mitochondrial function analysis

Mitochondrial respiratory chain enzyme activities were determined as previously described (Wibom et al., 2002). Mitochondrial oxygen consumption measurements of NES cells were performed on intact cells, using an Oroboros oxygraph (Oroboros Instruments GmbH). Maximal respiration was measured by titration of mitochondrial uncoupler CCCP or 2,4-Dinitrophenol (DNP).

RNAseq analysis

Total RNA from CCo1&2^{NES} and KO1&2^{NES} clones at 0 or 4 days differentiation was obtained as previously described. RNA quality was confirmed using a Bioanalyser 2100 (Agilent). Samples with a minimum RNA integrity number (RIN) of 8.5 were used. Sequencing was performed using Illumina HiSeq 2500, High Output V4 chemistry, PE (paired-end) 2x125bp in 1 lane. The library method used was Illumina TruSeq Stranded mRNA, Poly-A selection (200 ng used for each library). Sequencing was performed by the SciLife Laboratory NGI core facility (Science for Laboratories, Stockholm, Sweden). The reads were mapped using Tophat2 (Kim et al., 2013)

to the human reference assembly, version GRCh38. Principal component analysis of the transcriptomic data from all samples showed that KO3[NES] did not cluster with its corresponding genetic matches both in the undifferentiated and differentiated state (Figure S5D and E). This clone showed poor growth in culture, and further inspection revealed that DNA replication pathways were repressed (Figure S5F). We removed this clone from all analysis, as it probably was compromised during CRISPR/Cas9 gene editing and/or expansion.

Proteomic analysis

Proteomics analysis was performed on control NES cells, KO1&2[NES], CCo1&2[NES] as wells as Pat1[NES] cells. Samples were lysed by the addition of ProteaseMax/Urea and sonicated. Peptides were separated on a homemade C18 column, 25 cm (Silica Tip 360 μm OD, 75 μm ID, New Objective, Woburn, MA, USA) with a 120 min gradient at a flow rate of 300 nl/min. The gradient went from 5-26% of buffer B (2% acetonitrile, 0.1% formic acid) in 120 min and up to 95% of buffer B in 5 min and injected onto the LC-MS/MS system (UltimateTM 3000 RSLCnano chromatography system and Q Exactive Plus Orbitrap mass spectrometer (Thermo Fisher Scientific). Proteomics analysis was performed by the Karolinska Institute proteomics core facility. Analysis of principal component one and two did not reveal outliers (Figure S5G), therefore all samples were included for further analysis.

Neuronal morphology analysis

Neuronal body area and neuronal processes number and width emerging from neuronal bodies were measured using ZEN 2011 software. Images were acquired using Axio Imager2 fluorescence microscope from Carl Zeiss. For the number of neuronal processes, a minimum threshold of 10 μm width was introduced in order to clarify the morphological changes found.

Sholl analysis

Sholl analysis was performed with Simple Neurite Tracer (Longair et al., 2011) and a semi-automated tool for Fiji (Schindelin et al., 2012) in control NES cells, Pat1[NES], Pat2[NES], CCo1[NES] and KO1[NES] cells after 3 weeks of differentiation.

QUANTIFICATION AND STATISTICAL ANALYSIS

RNASeq and proteomics data analysis

Data analysis was performed with R (v3.3.2) (R Core Team (2013)), the supplementary code for statistical analysis and figures is provided. Mapped RNAseq count files were cleaned by removing all genes with raw counts of less than 3 per one million counts. Mapped proteins were only included if its peptides were detected across all samples. Data were then normalised on the total amount of reads per sample and statistically analysed with DESeq 2 (v1.14.1) of the Bioconductor tools without log2-fold change shrinkage (betaPrior = FALSE) by applying a Wald-test (Love et al., 2014). Adjusted p-values were calculated applying individual hypothesis weighting (Ignatiadis et al., 2016). Gene set enrichment analysis (GSEA) was performed on the Broad Institute GSEA Java platform against libraries (Subramanian et al., 2005), Hallmarks, KEGG, Biocarta, Reactome, all v5.2, which were also used to extract genes associated to OXPHOS-related pathways. Discrepancies of normalised enrichment scores between proteomic and transcriptomic GSEA data could be explained by the much larger sequencing depth of RNAseq (>13,237 accepted hits) compared to mass spectrometry (3058 accepted hits). Ontologies were identified

with WebGestalt (Wang et al., 2013). Human Gene Atlas comparisons were done in EnrichR (Kuleshov et al., 2016).

All parameters in our study were distributed normally. Experiments were performed at least three times when statistical tests applied. Data are expressed as mean ± standard deviation (SD) and differences were tested by a two-tailed t-test. The values P < 0.05 were considered statistically significant. Other types of analysis are indicated in the text. For confirmation of RNAseq or proteomics analysis experiments were repeated twice.

DATA AVAILABILITY

RNAseq raw data files and processed data are publicly available at GEO: GSE99559.

Proteomics raw data files and processed data are publicly available at PRIDE: PXD006647.

REFERENCES

Chambers, S.M., Fasano, C.A., Papapetrou, E.P., Tomishima, M., Sadelain, M., Studer, L., 2009. Highly efficient neural conversion of human ES and iPS cells by dual inhibition of SMAD signaling. Nat Biotechnol 27, 275–280. doi:10.1038/nbt.1529

Cong, L., Ran, F.A., Cox, D., Lin, S., Barretto, R., Habib, N., Hsu, P.D., Wu, X., Jiang, W., Marraffini, L.A., Zhang, F., 2013. Multiplex genome engineering using CRISPR/Cas systems. Science 339, 819–823. doi:10.1126/science.1231143

Falk, A., Koch, P., Kesavan, J., Takashima, Y., Ladewig, J., Alexander, M., Wiskow, O., Tailor, J., Trotter, M., Pollard, S., Smith, A., Brüstle, O., 2012. Capture of neuroepithelial-like stem cells from pluripotent stem cells provides a versatile system for in vitro production of human neurons. PLoS ONE 7, e29597. doi:10.1371/journal.pone.0029597

Haack, T.B., Ignatius, E., Calvo-Garrido, J., Iuso, A., Isohanni, P., Maffezzini, C., Lönnqvist, T., Suomalainen, A., Gorza, M., Kremer, L.S., Graf, E., Hartig, M., Berutti, R., Paucar, M., Svenningsson, P., Stranneheim, H., Brandberg, G., Wedell, A., Kurian, M.A., Hayflick, S.A., Venco, P., Tiranti, V., Strom, T.M., Dichgans, M., Horváth, R., Holinski-Feder, E., Freyer, C., Meitinger, T., Prokisch, H., Senderek, J., Wredenberg, A., Carroll, C.J., Klopstock, T., 2016. Absence of the Autophagy Adaptor SQSTM1/p62 Causes Childhood-Onset Neurodegeneration with Ataxia, Dystonia, and Gaze Palsy. Am. J. Hum. Genet. 99, 735–743. doi:10.1016/j.ajhg.2016.06.026

Ignatiadis, N., Klaus, B., Zaugg, J.B., Huber, W., 2016. Data-driven hypothesis weighting increases detection power in genome-scale multiple testing. Nat Meth 13, 577–580. doi:10.1038/nmeth.3885

Kim, D., Pertea, G., Trapnell, C., Pimentel, H., Kelley, R., Salzberg, S.L., 2013. TopHat2: accurate alignment of transcriptomes in the presence of insertions, deletions and gene fusions. Genome Biol 14, R36. doi:10.1186/gb-2013-14-4-r36

Koch, P., Opitz, T., Steinbeck, J.A., Ladewig, J., Bruestle, O., 2009. A rosette-type, self-renewing human ES cell-derived neural stem cell with potential for in vitro instruction and synaptic integration. Proc. Natl. Acad. Sci. U.S.A. 106, 3225–3230. doi:10.1073/pnas.0808387106

Kuleshov, M.V., Jones, M.R., Rouillard, A.D., Fernandez, N.F., Duan, Q., Wang, Z., Koplev, S., Jenkins, S.L., Jagodnik, K.M., Lachmann, A., McDermott, M.G., Monteiro, C.D., Gundersen, G.W., Ma'ayan, A., 2016.

Enrichr: a comprehensive gene set enrichment analysis web server 2016 update. Nucleic Acids Res. 44, W90–7. doi:10.1093/nar/gkw377

Longair, M.H., Baker, D.A., Armstrong, J.D., 2011. Simple Neurite Tracer: open source software for reconstruction, visualization and analysis of neuronal processes. Bioinformatics 27, 2453–2454. doi:10.1093/bioinformatics/btr390

Love, M.I., Huber, W., Anders, S., 2014. Moderated estimation of fold change and dispersion for RNA-seq data with DESeq2. Genome Biol 15, 550. doi:10.1186/s13059-014-0550-8

Schindelin, J., Arganda-Carreras, I., Frise, E., Kaynig, V., Longair, M., Pietzsch, T., Preibisch, S., Rueden, C., Saalfeld, S., Schmid, B., Tinevez, J.-Y., White, D.J., Hartenstein, V., Eliceiri, K., Tomancak, P., Cardona, A., 2012. Fiji: an open-source platform for biological-image analysis. Nat Meth 9, 676–682. doi:10.1038/nmeth.2019

Subramanian, A., Tamayo, P., Mootha, V.K., Mukherjee, S., Ebert, B.L., Gillette, M.A., Paulovich, A., Pomeroy, S.L., Golub, T.R., Lander, E.S., Mesirov, J.P., 2005. Gene set enrichment analysis: A knowledge-based approach for interpreting genome-wide expression profiles. Proc. Natl. Acad. Sci. U.S.A. 102, 15545–15550. doi:10.1073/pnas.0506580102

Wang, J., Duncan, D., Shi, Z., Zhang, B., 2013. WEB-based GEne SeT AnaLysis Toolkit (WebGestalt): update 2013. Nucleic Acids Res. 41, W77–83. doi:10.1093/nar/gkt439

Wibom, R., Hagenfeldt, L., Dobeln, von, U., 2002. Measurement of ATP production and respiratory chain enzyme activities in mitochondria isolated from small muscle biopsy samples. Anal. Biochem. 311, 139–151.

Wu, S., Johansson, J., Damdimopoulou, P., Shahsavani, M., Falk, A., Hovatta, O., Rising, A., 2014. Spider silk for xeno-free long-term self-renewal and differentiation of human pluripotent stem cells. Biomaterials 35, 8496–8502. doi:10.1016/j.biomaterials.2014.06.039